Computers and Geotechnics 194 (2026) 107997

Contents lists available at ScienceDirect

Computers and Geotechnics

journal homepage: www.elsevier.com/locate/compgeo

Research Paper

Advanced hypoplastic contact modelling of field tests for tension piles in layered soils

D. Alkateeb *, J. Grabe

Institute of Geotechnical Engineering and Construction Management, Hamburg University of Technology (TUHH), Schellerdamm 22, Hamburg, 21079, Germany

ARTICLE INFO

Keywords:
Tensile capacity
Hypoplastic contact model
Finite-element analysis
Layered soils
Pile-soil interaction
Torsional shear test

ABSTRACT

Conventional Coulomb friction models often fail to reproduce the complete non-linear load–displacement response of soil–pile interfaces, particularly during unloading–reloading sequences. Advanced hypoplastic contact formulations address these limitations by capturing pressure dependency (barotropy), density dependency (pyknotropy), and surface roughness effects using the same constitutive parameter set as the surrounding soil continuum. This study presents the first three-dimensional back-analysis of a hypoplastic contact model benchmarked against full-scale tensile load tests on steel H-piles in a complex, 23-layer stratified soil profile. The methodology establishes a physically consistent calibration framework where the interface roughness parameter is derived directly from torsional interface shear tests on pile-specific steel, rather than empirical estimation. These same contact formulations are subsequently applied to simulate the laboratory tests, ensuring consistency between calibration and field-scale prediction. The model accurately reproduces the field response and reduces the root mean square error (RMSE) by 71% relative to the Coulomb model, capturing hysteretic loops that simplified models miss. A parametric sensitivity analysis identifies interface roughness and pile circumference as the dominant capacity drivers, while relative density and in-situ earth pressure exert a moderate influence. The results demonstrate that physically based contact formulations are essential for accurate pile-soil interaction modelling in complex profiles, enabling more reliable and economical foundation design.

1. Introduction

Reliable prediction of the tensile bearing capacity of driven steel piles in layered soils remains a significant challenge in geotechnical practice. Although empirical, semi-empirical, and analytical approaches are widely employed, they predominantly rely on simplified assumptions regarding soil behaviour and pile-soil interaction. Consequently, they often fail to capture the complex mechanical mechanisms developing at the pile-soil interface (Alkateeb and Grabe, 2022, 2026). These simplifications have non-trivial implications, potentially leading to considerable discrepancies between predicted and actual bearing capacities. This uncertainty can result in uneconomically conservative designs or, conversely, introduce latent safety risks. Therefore, developing more accurate numerical models is not only of scientific interest but also of direct practical relevance for ensuring the economic efficiency and safety of geotechnical structures.

Numerical analyses frequently employ simplified contact models (Stapelfeldt et al., 2020; Bienen et al., 2021; Dao et al., 2023; Dao and Grabe, 2024; Alkateeb and Grabe, 2026). While adequate for applications where contact mechanics are secondary, these models prove insufficient for complex soil–structure interactions where the interface behaviour governs the system response (Ghionna and Mortara, 2002; Weißenfels and Wriggers, 2015; Stutz et al., 2016; Weißenfels et al., 2017; Stutz and Wuttke, 2018; Staubach et al., 2022a; Alkateeb and Grabe, 2026). A realistic prediction of shaft resistance therefore requires a contact formulation that evolves with normal stress level, density state, and loading history.

These limitations were notably highlighted in a recent Class-A prediction reported by Alkateeb and Grabe (2026) for full-scale tensile load tests on steel H-piles at Niederfinow, Germany. The prediction employed a conventional elasto-plastic friction model at the pile-soil interface and showed limited agreement with the measured field response, especially during unloading and reloading. This inadequacy was notable, given that the surrounding soil continuum was described by an advanced hypoplastic constitutive model, demonstrating that a high-quality continuum model does not compensate for an overly idealised interface law.

* Corresponding author.
E-mail address: diaa.alkateeb@tuhh.de (D. Alkateeb).

https://doi.org/10.1016/j.compgeo.2026.107997
Received 27 November 2025; Received in revised form 12 January 2026; Accepted 12 February 2026
Available online 23 February 2026
0266-352X/© 2026 The Authors. Published by Elsevier Ltd. This is an open access article under the CC BY license (http://creativecommons.org/licenses/by/4.0/).

Motivated by these findings, this study employs an advanced hypoplastic contact formulation to perform a physically grounded back-analysis of the Niederfinow field tests. Crucially, the interface parameters are calibrated against dedicated experiments using a torsional interface shear tester to ensure physical validity. Two hypoplastic formulations are evaluated: the model by Arnold and Herle (2006) and the enhanced formulation by Stutz et al. (2016). Their performance is comparatively evaluated in Section 4.5.4 to select the most efficient approach for the full-scale model.

1.1. State of research on contact modelling

Unlike simplified approaches, advanced, physically based contact models, such as hypoplasticity, offer a more sophisticated basis for analysis. They can realistically capture complex interface phenomena such as pressure dependency (barotropy), density dependency (pyknotropy), and the influence of surface roughness using the same parameter set as the surrounding soil continuum. The development of such advanced models has undergone significant evolution.

For the numerical modelling of mechanical interface behaviour, two fundamental approaches exist: specific contact models, which focus purely on friction modelling, and the application of modified continuum models for the soil within a thin interface layer. While traditional contact models are typically limited to describing normal and shear stresses, the continuum approach requires a complete tensorial representation of the stress and strain state. In the historical development since the 1970s, specific interface formulations were predominantly introduced, including non-linear elastic (Clough and Duncan, 1971; Gómez et al., 2003), elasto-plastic (Gens et al., 1989; Ghionna and Mortara, 2002; Fakharian and Evgin, 2000; Hamid and Miller, 2008; Shahrour and Rezaie, 1997; Hu and Pu, 2004; Staubach et al., 2022c,b), state-dependent plasticity models (Liu et al., 2006; Nakayama, 2006; Liu and Ling, 2008; Lashkari, 2013), damage mechanics (Hu and Pu, 2003), and disturbed-state concepts (Navayogarajah et al., 1992; Samtani et al., 1996; Shao and Desai, 2000).

Modified continuum models offer the advantage of efficient implementation without the complete reformulation of the constitutive model (Arnold and Herle, 2006; Weißenfels and Wriggers, 2015; Weißenfels et al., 2017; Stutz et al., 2017; Staubach et al., 2022c). Apart from surface roughness and shear zone thickness, no additional parameters are required, as these typically align with the continuum model parameters. Calibration can often be performed without specific interface shear tests, as the shared constitutive parameters are derived from the standard calibration of the continuum soil model using common laboratory tests. Only a few interface-specific parameters, such as surface roughness, need to be estimated, often from literature or empirical guidelines.

Despite various approaches, only a few three-dimensional contact models exist (Liu et al., 2014; Fakharian and Evgin, 2000; Gennaro and Frank, 2002; Hu and Pu, 2003; Costa D Aguiar et al., 2011; Arnold and Herle, 2006; Arnold, 2008; Duriez and Vincens, 2015; Stutz et al., 2017; Staubach et al., 2022c), and their implementation in commercial finite element (FE) software remains challenging. A promising continuum approach for solving complex contact problems involves using modified continuum models based on hypoplasticity (Arnold and Herle, 2006; Arnold, 2008; Stutz et al., 2017; Staubach et al., 2022c). The first one-dimensional form of a hypoplastic contact model was presented by Herle and Nübel (1999). Gutjahr (2003) adapted the hypoplastic model by von Wolffersdorff (1996) for simulations of structure-soil interactions. Arnold and Herle (2006) achieved a major advancement with the development of the first three-dimensional hypoplastic contact model, assuming identical normal stress components in the contact elements. Stutz et al. (2016) extended this approach by considering different normal stress components in the contact element. A further refinement was introduced by Staubach et al. (2022c), who developed a method in which the stresses and strains in the plane are not directly coupled with each other but are instead connected to the adjacent soil in the finite element method (FEM). This approach allows all normal stresses to have different values. Niebler et al. (2025) extended existing hypoplastic contact models by developing an approach that realistically simulates the experimentally observed continuous transition between sticking and slipping (“stick–slip transition”) at the interface. This model extension accounts for surface roughness, normal stress, and density state.

1.2. Objectives and contributions of this work

While advanced hypoplastic interface formulations are available in the literature (e. g., Arnold and Herle, 2006; Stutz et al., 2017; Staubach et al., 2022c), their application has been largely confined to laboratory experiments and small-scale model tests in homogeneous conditions due to numerical stability issues in complex boundary value problems. This study overcomes these barriers by presenting the first three-dimensional implementation of a hypoplastic contact formulation for full-scale tension pile analysis in highly stratified soils (23 distinct layers). The work moves beyond simple “application” to demonstrate the applicability and the necessity of hypoplastic interfaces in complex, real-world geotechnical scenarios where conventional methods systematically fail to reproduce the measured field response.

Accordingly, the overarching objective of this study is to conduct a physically grounded back-analysis of a full-scale pile pull-out test in strongly layered ground and to quantify where and why an advanced hypoplastic interface provides added value over a conventional Coulomb law under identical modelling assumptions. The analyses benchmark the complete load–displacement path, including unloading–reloading stiffness and hysteresis, and quantify the trade-off between predictive accuracy and computational effort. The specific contributions of this study are as follows:

- This study presents the first implementation of hypoplastic contact models into complex full-scale field tests in a highly stratified soil profile (23 distinct layers). We focus on conditions where advanced interface behaviour (including unloading–reloading stiffness and hysteresis) governs the response, moving beyond the idealised homogeneous benchmarks typical of current literature.
- We establish a physically rigorous calibration methodology where the critical interface roughness (κ) is derived from dedicated torsional interface shear tests on pile-specific steel, rather than from empirical estimation. This explicitly links micro-scale laboratory behaviour to macro-scale field response.
- We detail the practical pathway for coupling the hypoplastic interface to Abaqus via `FRIC–UMAT` subroutines, addressing the numerical stability issues (convergence, singular points) that typically prevent the use of such advanced models at field scale.
- We quantify the model’s improved accuracy compared to the conventional Coulomb friction model within this specific geotechnical context, highlighting the trade-off between computational cost and predictive precision.
- We present a parametric analysis that illustrates the influence of key physical parameters (interface roughness κ, soil relative density I_D, virtual shear zone thickness d_s, earth pressure coefficient K_0, and pile circumference $U_{profile}$) as well as the numerical discretisation in large-scale simulations.

This work contributes to the literature by establishing a physically consistent and reproducible framework that transitions from laboratory-scale interface characterisation to full-scale numerical prediction in complex, stratified ground. The comparison with full-scale field data demonstrates the model’s predictive capabilities and supports its implementation for developing more reliable and economical design methods for pile foundations.

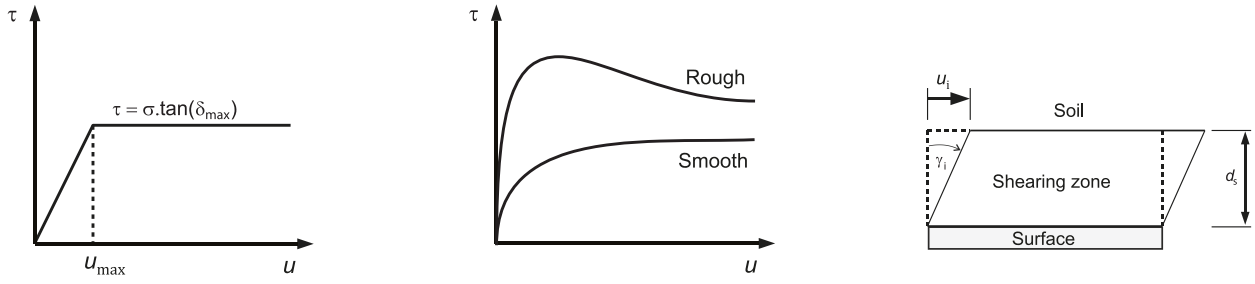

Fig. 1. Schematic representation of shear behaviour at contact interfaces: (a) idealised Coulomb friction model showing maximum shear stress (τ_{max}) at a limit displacement (u_{limit}); (b) realistic shear stress (τ) vs. displacement (u) response for rough and smooth surfaces; and (c) geometric relationship between shear zone thickness (d_s), displacement (u_i), and shear strain (γ_i).
Source: Modified from Arnold and Herle (2006).

2. Constitutive contact behaviour

In standard geotechnical modelling, the elasto-plastic Coulomb friction model is common. In this framework, the maximum tangential contact stress is proportional to the normal stress, as depicted in Fig. 1(a). This model defines a critical relative displacement u_{limit}, beyond which the maximum tangential contact stress is reached, and a transition to the sliding state occurs. However, this formulation represents a significant idealisation of the actual contact behaviour, as shown in Fig. 1(b). The differing mechanical behaviour is strongly influenced by the surface roughness, as shown in Fig. 1(b), which arises primarily from the nature of the shear zone d_s that develops at the interface. For very rough surfaces, the behaviour is analogous to that of dense sand in shear tests, where a thicker shear band forms, leading to a peak strength followed by gradual softening. Conversely, for smoother surfaces, the contact friction is mobilised over a much shorter shear path along a thinner shear band and tends to remain almost constant thereafter. The geometric relationship between the interface displacement u_i, the resulting shear strain γ_i, and the shear zone thickness d_s is illustrated in Fig. 1(c).

The hypoplastic contact model provides a substantial improvement by enabling a more accurate description of the complex soil–structure interactions. Compared to the idealised Coulomb model, it represents the actual contact behaviour much more realistically. The model is based on the fundamental insight that the behaviour of granular soils in the contact zone parallels that of a continuum, with surface roughness acting as the decisive parameter for shear behaviour.

2.1. Hypoplastic interface model by Arnold and Herle (2006)

The hypoplastic contact model was developed from the general form of the hypoplastic constitutive law for soils (von Wolffersdorff, 1996), with full equations provided in Appendix A. The fundamental relationship from which the contact model is adapted is given by:

$$\overset{\circ}{\mathbf{T}} = \mathbf{L} : \boldsymbol{D} + \mathbf{N}\,\|\boldsymbol{D}\|\,, \tag{1}$$

where $\overset{\circ}{\mathbf{T}}$ is the objective stress rate tensor and $\boldsymbol{D}$ is the strain rate tensor. Here, $\mathbf{L}$ and $\mathbf{N}$ symbolise linear and non-linear components of stiffness, respectively, expressed as:

$$\mathbf{L} = f_b f_e \frac{1}{\mathrm{tr}(\hat{\mathbf{T}}\cdot\hat{\mathbf{T}})}(F^2\mathbf{I} + a^2\hat{\mathbf{T}}\hat{\mathbf{T}})\,, \tag{2}$$

$$\mathbf{N} = f_b f_e f_d \frac{a\cdot F}{\mathrm{tr}(\hat{\mathbf{T}}\cdot\hat{\mathbf{T}})}(\hat{\mathbf{T}} + \hat{\mathbf{T}}^*)\,, \tag{3}$$

where F is the Matsuoka-Nakai failure condition, a is a model parameter, and f_b, f_e, f_d are factors accounting for barotropy and pyknotropy.

Arnold and Herle (2006) extended these equations for the hypoplastic contact model by introducing the roughness parameter κ of the contact surface. In the original formulation, κ is defined as the ratio of the maximally mobilised interface friction angle δ_{max} to the soil internal friction angle φ (Arnold, 2008; Stutz, 2016):

$$\kappa = \frac{\delta_{max}}{\varphi}\,. \tag{4}$$

In the present study, κ is evaluated using the critical-state plateau to obtain a transferable roughness parameter, i.e. $\kappa = \delta_{cs}/\varphi_{cs}$, where δ_{cs} is the critical-state interface friction angle and φ_{cs} is the critical-state internal friction angle of the adjacent soil.

Here, $0 < \kappa \leq 1$, with $\kappa = 1$ representing a perfectly rough surface. This parameter can be determined from interface shear tests, estimated from literature, or obtained through back-analysis. The Matsuoka–Nakai condition is given by Arnold and Herle (2006) as:

$$F = \sqrt{1 - \frac{9}{4}\left(\bar{\tau}_x^2 + \bar{\tau}_y^2\right)} - \frac{\sqrt{3}}{2}\sqrt{\bar{\tau}_x^2 + \bar{\tau}_y^2}\,. \tag{5}$$

In addition, Arnold and Herle (2006) proposed a modified parameter a following the suggestion of Herle and Nübel (1999) that the correct behaviour of the interface zone at critical state can be modelled by:

$$a = 3\sqrt{\frac{1}{2\tan^2\left(\kappa\varphi_c\right)} - \frac{1}{8}} - \frac{\sqrt{3}}{2\sqrt{2}}\,. \tag{6}$$

To adjust the mobilisation of shear stresses to match experimental results, they introduced an additional coefficient f_c, which is expressed as:

$$f_c = \frac{1}{\kappa}\,. \tag{7}$$

Incorporating these modifications, the final vectorial form of the hypoplastic contact model equation becomes:

$$\overset{\circ}{\mathbf{T}} = f_c(\mathbf{L} : \boldsymbol{D} + \mathbf{N}\,\|\boldsymbol{D}\|)\,. \tag{8}$$

For the calculation of the contact stresses, a virtual shear zone thickness d_s is introduced, corresponding to the actual thickness of the developing shear band at the contact surface (Fig. 1(c)). This virtual thickness d_s also depends on the surface roughness, density state, and mean grain size d_{50}. Eq. (9) defines the dependency of shear zone thickness on shear strain and displacement:

$$\tan\gamma_i = \frac{u_i}{d_s}\,. \tag{9}$$

Reports in the literature indicate that d_s can vary between $7\,d_{50}$ and $20\,d_{50}$ depending on the roughness of the surface and the adjacent soil conditions (Teichmann, 1989; Tejchman and Wu, 1995; Maier, 2002; Arnold and Herle, 2006). Other laboratory studies point to a typical shear zone thickness of approximately $5-10\,d_{50}$ at soil–structure

Table 1
Conceptual and practical comparison of the Coulomb and hypoplastic contact models, contrasting their ability to represent key physical soil behaviours and their respective implementation requirements.

Property	Coulomb contact model	Hypoplastic contact model
Barotropy (Pressure dependency)	× Not considered	✓ Fully considered
Pyknotropy (Density dependency)	× Not considered	✓ Fully considered
Surface roughness	× Simplified (Constant friction angle δ)	✓ Explicitly modelled (Roughness parameter κ and shear zone thickness d_s)
Shear stress development	Linear-elastic, perfectly plastic ($\tau_{max} = \sigma \cdot \tan\delta$)	Non-linear, stress- and density-dependent
Softening/hardening	× Not considered	✓ Captures peak, critical state, and softening/hardening response
Parameters	Friction coefficient μ, elastic slip stiffness	Interface (κ, d_s), and shared continuum parameters
Application range	Simple geotechnical contact problems	Complex soil–structure interaction, cyclic loading
Implementation complexity	✓ Simple (often standard in FE software)	× Advanced (requires user subroutines, e. g., FRIC–UMAT)
Computational cost	✓ Generally low	× Higher due to constitutive complexity and potentially more iterations

interfaces (Hu and Pu, 2004; DeJong et al., 2006; DeJong and Westgate, 2009; Martinez et al., 2015). Given this variability, a more precise value is often determined by calibrating d_s through the back-analysis of shear test data (Arnold and Herle, 2006). This procedure typically involves first adjusting the interface roughness parameter κ to match the measured reference shear stress level in the interface tests (either the peak value or the critical-state plateau). Subsequently, d_s is calibrated, as it functions as a scaling parameter for the shear displacement required to mobilise that reference stress (Arnold, 2008).

In the model by Arnold and Herle (2006), the stress and strain rate tensors are reduced to a vectorial form, assuming equal normal stresses in the contact plane:

$$\boldsymbol{\sigma} = \begin{bmatrix} \sigma_n \\ \sigma_n \\ \tau_x \\ \tau_y \end{bmatrix} \qquad \dot{\boldsymbol{\epsilon}} = \begin{bmatrix} \dot{\epsilon}_n \\ \dot{\epsilon}_n \\ \dot{\gamma}_x/2 \\ \dot{\gamma}_y/2 \end{bmatrix}. \tag{10}$$

2.2. Hypoplastic interface model by Stutz et al. (2016)

Stutz et al. (2016) extended the approach of Arnold and Herle (2006) by developing a more general framework that allows for different normal stress components at the interface. This modification assumes an oedometric condition at the interface, where the in-plane stress (σ_p) can develop independently of the normal stress (σ_n) during shear. This is achieved by using reduced stress and strain rate tensors that simulate simple shear conditions, where the in-plane strain rate is zero ($\dot{\epsilon}_p = 0$):

$$\boldsymbol{\sigma} = \begin{bmatrix} \sigma_n \\ \sigma_p \\ \tau_x \\ \tau_y \end{bmatrix} \qquad \dot{\boldsymbol{\epsilon}} = \begin{bmatrix} \dot{\epsilon}_n \\ 0 \\ \dot{\gamma}_x/2 \\ \dot{\gamma}_y/2 \end{bmatrix}. \tag{11}$$

This formulation better represents the stress state in a thin shear zone and can be implemented efficiently by using the full 3D soil model as a constitutive driver for a frictional subroutine, requiring only the transformation of the stress and strain tensors (Stutz et al., 2017). Unlike the basic implementation of Arnold's model, the framework proposed by Stutz et al. (2016) is capable of coupling with the full constitutive soil driver, potentially including the intergranular strain extension if required. A comparative performance assessment of these two formulations is presented in Section 4.5.4 to justify the selection for the full-scale analysis.

2.3. Numerical implementation of the hypoplastic contact models

The theoretical foundation of the hypoplastic contact model enables the comprehensive capture of essential soil properties, such as barotropy (pressure dependency), pyknotropy (density dependency), progressive softening during shear, and the influence of surface roughness. These properties cannot be captured by the classic Coulomb model, which limits its applicability to a restricted number of geotechnical problems. Table 1 summarises the essential differences between the Coulomb and hypoplastic contact models.

A notable practical advantage of the implemented hypoplastic contact model over other specialised contact models is the use of the same parameterisation as that for the surrounding soil. The only interface-specific parameters are the friction parameter κ and the virtual shear zone thickness d_s. The roughness parameter κ controls the stress mobilisation and depends on the normalised roughness R_n, with R_{max} representing the maximum surface roughness. This facilitates reliable Class-A predictions (Stutz et al., 2017) and has been successfully applied in numerous studies (Gutjahr, 2003; Arnold and Herle, 2006; Stutz et al., 2016; Staubach et al., 2022c; Niebler et al., 2025).

The model is implemented in Abaqus by coupling the `FRIC` and `UMAT` subroutines (Dassault Systèmes, 2022). Here, the material model of the soil is modified to account for surface roughness. The required tensor components are provided by the friction subroutine (`FRIC` keyword in Abaqus), which calls the user-defined material subroutine (`UMAT`). This approach enables efficient integration without requiring complete reimplementation and ensures a consistent representation of the soil–structure interaction (Stutz et al., 2017).

The model by Arnold and Herle (2006) uses an explicit forward-Euler integration scheme with adaptive sub-stepping to update the interface stresses. For completeness, the detailed algorithm is provided in Appendix B. The more advanced model by Stutz et al. (2016) was implemented using an implicit update scheme, also detailed in Appendix B as Algorithm 2. This method employs a local Newton–Raphson iterative loop within each time increment.

3. Full-scale tensile load tests at niederfinow

The numerical model is benchmarked against full-scale static tensile load tests on driven steel H-piles conducted at the Niederfinow test site (Germany). The HP 320 x 88.5 test piles feature a length of 18.8 m, an embedment depth of 18.3 m, and a pile head extending 0.5 m

above ground level. The piles were installed using a combined driving procedure, where the first 6 m were installed by vibratory driving followed by impact driving for the remaining embedment to reach the final depth. The load tests were carried out after a waiting period of five weeks to allow for pore pressure dissipation and soil set-up. The applied loading history follows the field procedure and includes an initial loading stage up to 400 kN, followed by unloading and reloading up to failure, which enables a direct assessment of unloading–reloading stiffness and hysteresis in addition to ultimate resistance. During testing, the pile head load was measured using a calibrated load cell and the vertical displacement was recorded using multiple displacement gauges with high resolution, providing a reliable load–displacement curve for model comparison. In addition, the test piles were instrumented with high-resolution fibre-optic strain measurements along the pile shaft, enabling detailed strain (and thus load-transfer) profiling during the load test and supporting a mechanistic interpretation of the field response (Alkateeb and Grabe, 2026).

The Niederfinow programme offers well-defined boundary conditions for numerical back-analysis: the stratigraphy is strongly heterogeneous, and the test includes a complete loading–unloading–reloading sequence rather than a monotonic proof load. The soil profile is described in detail in Section 4.3. The initial state is constrained by site investigation data (boreholes and CPT profiles), which reduces modelling freedom and allows the interface formulation to be tested in a genuinely predictive manner.

Although multiple piles and load tests were carried out within the wider site programme, this paper intentionally focuses on the most comprehensively documented tensile test for which a consistent loading protocol and high-resolution pile-head load–displacement data are available. This "single-case" back-analysis is therefore not intended as a statistical validation across many tests; instead, it constitutes a focused, mechanistic full-scale implementation and back-calculation with the hypoplastic contact formulation, demonstrating its ability to reproduce the complete non-linear load–displacement response, including unloading–reloading stiffness and hysteresis, in a highly stratified profile under well-constrained boundary conditions. A crucial distinction of this assessment is that the key interface parameter κ was derived independently from laboratory tests on pile steel, rather than being back-fitted to the pile test itself. Comparable public datasets for such complex tests, featuring high-resolution instrumentation (including fibre-optic strain measurements) and detailed stratigraphic definition, are currently scarce. The Niederfinow test is exceptional in terms of boundary-condition definition and measurement quality, enabling a stringent assessment of the interface formulation under realistic heterogeneous conditions. Future work should extend the comparison to additional piles, loading histories, and installation modelling (including models that incorporate installation effects), once sufficiently complete datasets become available. For additional details on the field testing campaign and site conditions, reference is made to Alkateeb and Grabe (2026).

4. Numerical model

This section describes the three-dimensional finite element model developed in Abaqus/Standard 2023 to simulate the interaction between the pile and the soil. The model implementation, including geometry, boundary conditions, and material properties, is described below. To ensure quality, the simulation results are first assessed using the statistical methods outlined in the following subsection.

4.1. Statistical evaluation metrics

The numerical simulations are compared with experimental data using complementary statistical methods. For the objective quantification of model quality, two error metrics are employed: mean absolute percentage error (MAPE) for relative assessment and root mean square error (RMSE) for absolute measurement. The MAPE is defined as:

$$\mathrm{MAPE} = \frac{100\%}{n} \sum_{i=1}^{n} \left| \frac{\varepsilon_i^{\mathrm{exp}} - \varepsilon_i^{\mathrm{sim}}}{\varepsilon_i^{\mathrm{exp}}} \right| , \tag{12}$$

where n represents the number of measurement points, $\varepsilon_i^{\mathrm{exp}}$ denotes the experimental measurements, and $\varepsilon_i^{\mathrm{sim}}$ indicates the corresponding numerical results. This metric enables a percentage assessment of the prediction accuracy across the entire load range. To capture absolute deviations, RMSE is utilised:

$$\mathrm{RMSE} = \sqrt{\frac{1}{n} \sum_{i=1}^{n} (\varepsilon_i^{\mathrm{exp}} - \varepsilon_i^{\mathrm{sim}})^2} . \tag{13}$$

The RMSE quantifies the mean square deviation in units of the measured values, with larger discrepancies weighted disproportionately through squaring. This dual approach enables a differentiated assessment of model quality in terms of both relative and absolute deviations. When analysing pile bearing behaviour across different soil layers and multiple load levels, this combined evaluation provides meaningful indicators for assessing the predictive quality of both implemented contact models.

4.2. Geometry and boundary conditions

The numerical analysis of the pile load tests is performed using the finite element programme Abaqus/Standard 2023. The simulation utilises Lagrangian elements and implicit time integration to calculate the tensile bearing capacity of the driven steel piles. Implicit time-integration methods are preferred due to their unconditional stability, which allows for equilibrium solutions within each increment, thereby permitting larger time steps than explicit methods.

The numerical model (Fig. 2) consists of a quarter of the system with a length of 10 m and a height of 30 m, utilising double symmetry to reduce the computational effort. Symmetry boundary conditions are applied to the two vertical inner faces of the quarter model, restricting the motion and rotation on the respective planes of symmetry (x-z and y-z). To simulate a semi-infinite soil domain, displacement normal to the far-field vertical boundaries is prevented, and the model's base is fully fixed. The model is discretised with 74,488 continuum elements of type C3D8R with reduced integration and enhanced hourglass control. The mesh density is refined in the vicinity of the pile to capture the complex stress and deformation states in the contact zone with high precision. The dimensions of the soil domain correspond to a horizontal distance of 33 times the pile width and a vertical model height of 1.6 times the pile length, ensuring that boundary influences are minimised.

For the HP 320 x 88.5 pile, linear-elastic behaviour of S355 steel is assumed. The FE geometry follows the field-test configuration (Section 3), with a total pile length of 18.8 m, an embedment depth of 18.3 m, and a pile-head projection of 0.5 m above ground level. The pile is modelled as pre-installed "wished-in-place", meaning installation effects and subsequent time-dependent set-up are not explicitly considered in this study.

Pile driving typically induces cavity expansion effects, increasing lateral earth pressure ($K > K_0$) and densifying the surrounding soil (Randolph, 2003). Explicitly modelling these large-deformation installation processes and subsequent time-dependent set-up (stress relaxation) is considered computationally prohibitive and methodologically challenging and is outside the scope of this study. The adoption of the at-rest earth pressure coefficient (K_0) is justified by the following considerations: H-piles are "low displacement" piles compared to closed-ended pipe piles, inducing less severe cavity expansion effects. Second, stress relaxation over time (set-up effects) (Skov, 1997; Chow et al., 1997; Axelsson, 2000; Grabe et al., 2014) often reduces driving stresses back towards geostatic levels (Grabe et al., 2014; Alkateeb and Grabe, 2026). Consequently, the geostatic stress state serves as

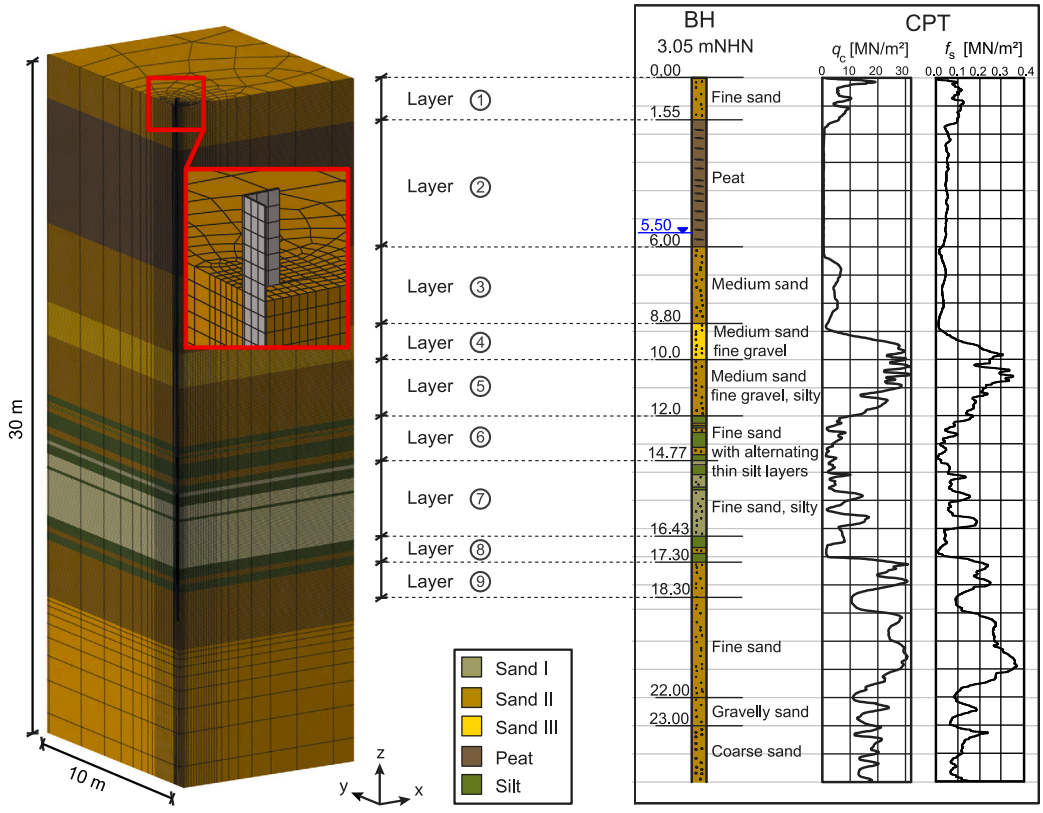

Fig. 2. Numerical model and discretisation of the quarter-symmetric FE model for calculating the pull-out bearing capacity (left) and soil structure, along with cone penetration test (CPT) data at the site of the pile load test (right).

Table 2
Loading sequence from the field tests, detailing the applied load ranges and corresponding measured pile head displacements for each phase.

Test phase	Load (kN)	Displacement (mm)
Loading	0–400	0–3.8
Unloading	400–7.0	3.8–1.3
Reloading	7.0–617	1.3–60.0

a valid, conservative lower bound. This approach effectively isolates the performance of the contact formulation from the uncertainties associated with installation modelling. By adopting a geostatic stress state, the analysis proves the validity of the static interface physics, providing a robust baseline upon which future studies can superimpose installation effects. The good agreement between simulation and field data suggests that, for these specific H-piles after a 5-week set-up period, residual installation stresses did not dominate the response, although this may not generalise to other pile types.

The geostatic stress state is initialised using earth pressure coefficients according to $K_0 = 1 - \sin(\varphi')$ following Jaky (1948). For peat, however, a value of $K_0 = 0.3$ is used based on Yamaguchi et al. (1985). In the second step, the self-weight of the pile is activated, and contact between the pile and soil is established. Finally, the pile is subjected to the path-controlled tensile loading sequence derived from the field tests (Alkateeb and Grabe, 2026). This sequence, which includes monotonic loading, unloading, and reloading phases, is detailed in Table 2.

4.3. Soil layering and material properties

The subsoil at the site is highly stratified, comprising approximately 23 distinct layers identified from borehole profiles and laboratory tests. To ensure the simulation accurately reflects in-situ conditions, all 23 layers were explicitly modelled in the numerical model geometry. However, for parameter assignment and descriptive clarity, this complex profile is grouped into nine representative material zones. The profile begins with fill material to a depth of 1.55 m, followed by a peat layer extending to 6 m. Below this are alternating layers of fine and coarse sand down to 12 m. The subsequent zones, nominally referred to as Layers 6 and 8, are particularly heterogeneous and were modelled as multiple, thinly inter-layered strata of fine sand and silt, exactly as found in the soil investigation. From 17.30 m to the final depth, coarse-grained sand was encountered. The characteristic properties and mechanical parameters of the primary soil types identified within these layers are summarised in Table 3. The grain size distribution curves of the considered sands are shown in Fig. 3. To establish a realistic initial state, the relative density (I_D) for each sand layer was derived from the in-situ cone penetration test (CPT) data in Fig. 2. The initial void ratios (e) in Table 3 are based on these layer-specific I_D values, which were calculated using the empirical correlation from Kulhawy and Mayne (1990), $I_D{}^2 = Q_{cn}/350$, where the normalised cone resistance, Q_{cn}, is defined as:

$$Q_{cn} = \frac{(q_c/p_a)}{(\sigma'_v/p_a)^{0.5}} \tag{14}$$

Here, q_c is the cone resistance, σ'_v is the effective vertical stress, and p_a is a reference pressure of 100 kPa. It is acknowledged that within the thinly inter-layered zones (Layers 6 and 8), CPT cone resistance (q_c) values may be slightly suppressed due to the "thin-layer effect" (smearing of q_c values in thin strata). No specific thin-layer correction factors were applied, meaning the derived I_D (and consequently stiffness) in Layers 6 and 8 may be underestimated by a small margin, resulting in a conservative interface response in these partial zones.

The mechanical behaviour of non-cohesive soils is described using the hypoplastic constitutive model according to von Wolffersdorff

Table 3
Summary of geotechnical parameters for the representative soil zones used in the numerical model. The values are based on laboratory testing and correlations with in-situ CPT data from the project site.

Layer No	Depth (m)	Soil	d_{50} (mm)	C_u (–)	q_c (MPa)	d_s (mm)	e (–)
1	<1.55	Sand II	0.23	2.3	8.0	4.6	0.67
2	1.55–6.0	Peat	–	–	0.5	–	2.72
3	6.0–8.8	Sand II	0.22	2.3	8.0	4.4	0.60
4	8.8–10.0	Sand III	0.33	2.7	25.0	6.6	0.50
5	10.0–12.0	Sand II	0.22	2.0	26.0	4.4	0.59
6	12.0–14.77	Silt/Sand II	–	–	3.0	–	–
7	14.77–16.43	Sand I	0.08	2.9	10.0	1.6	0.65
8	16.43–17.30	Silt/Sand I	–	–	3.0	–	–
9	>17.30	Sand II	0.22	1.7	28.0	4.4	0.57

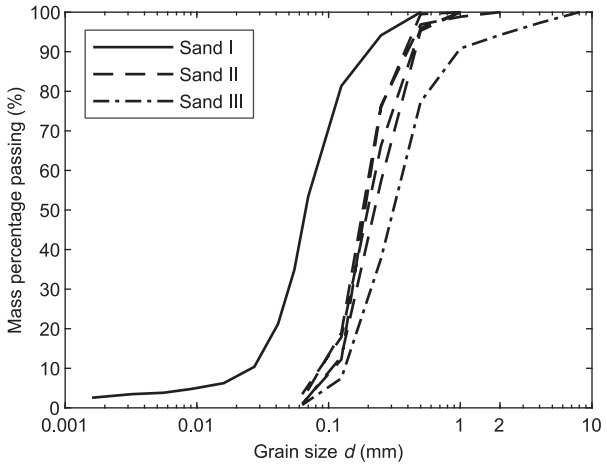

Fig. 3. Representative grain size distribution curves of the investigated sands.

Table 4
Parameters of hypoplasticity with intergranular strain extension for the investigated non-cohesive sands.

Parameter	Unit	Sand I	Sand II	Sand III
φ_c	(°)	32.8	31.2	30.1
h_s	(MPa)	1650	2442	2267
n	(–)	0.35	0.255	0.29
e_{d0}	(–)	0.48	0.47	0.37
e_{c0}	(–)	0.98	0.84	0.72
e_{i0}	(–)	1.12	0.97	0.83
α	(–)	0.055	0.09	0.15
β	(–)	1.56	1.65	1.3
m_T	(–)	1.46	1.53	1.17
m_R	(–)	4.68	4.52	4.65
R_{max}	(–)	$2.1 \cdot 10^{-4}$	$6.7 \cdot 10^{-4}$	$2.3 \cdot 10^{-4}$
β_R	(–)	0.16	0.58	0.8
χ	(–)	3.46	4.92	3.06

(1996), with the intergranular strain extension by Niemunis and Herle (1997). This high-quality constitutive model captures the essential properties of granular materials, including dilatancy, contractancy, varying loading and unloading stiffnesses, and the dependence of stiffness on stress state and relative density. For detailed information on the constitutive equations, please refer to Appendix A. The simulation assumes ideal drainage conditions for the non-cohesive soil layers. The hypoplastic model was calibrated by back-calculating Consolidated Drained triaxial (CD) and Constant Rate of Strain oedometer (CRS) tests on samples of various densities and stress levels. The results are shown in Figs. 4 and 5. Fig. 4 plots the deviatoric stress (q) against the axial strain (ε_1) for the triaxial tests. Correspondingly, Fig. 5 presents the axial strain (ε_1) versus the vertical stress (σ_1) from the CRS oedometer tests. The figures show good agreement between simulation and measurement. The determined parameter sets for the three characteristic sands are summarised in Table 4.

Table 5
Material parameters for cohesive layers.

Material	E (kPa)	ν (–)	φ' (°)	c'/c_u (kPa)	ψ (°)
Organic peat	1200	0.38	52	25	0
Silt (undrained)	4000	0.49	0	50	0

For the cohesive soil layers (peat and silt), an elasto-plastic constitutive model featuring the Mohr–Coulomb plasticity criterion is employed. This modelling choice is justified by the secondary influence of these layers on the overall tensile capacity, due to their limited extent and low CPT resistance ($q_c \approx 0.5$–3.0 MPa). A dedicated sensitivity analysis, performed by numerically excluding shaft resistance in these layers, confirmed that the combined contribution of the peat and silt layers to the total pile capacity is only about 6%. Using a simpler model is therefore computationally efficient and does not impact the study's primary findings, avoiding extensive calibration for little proportional benefit. The Mohr–Coulomb parameters for peat and silt, detailed in Table 5, were derived based on laboratory test results from Alkateeb and Grabe (2026). The relatively high effective friction angle of $\varphi' = 52°$ for the peat layer is consistent with findings for fibrous organic soils, where significant inter-particle locking of fibres enhances strength (Yamaguchi et al., 1985; Edil and Dhowian, 1981; Cola and Cortellazzo, 2005; Mesri and Ajlouni, 2007). The silt layers are specifically modelled under undrained conditions. The steel pile is modelled with linear-elastic material behaviour, with $E = 2.1 \cdot 10^8$ kPa and $\nu = 0.3$.

4.4. Pile-soil interaction

The contact between the pile and soil is modelled using a surface-to-surface formulation with "finite sliding". In the normal direction, a hard contact formulation is applied, which prevents penetration of the surfaces. The contact stiffness is automatically determined by the penalty method, which ensures a balanced compromise between numerical stability and physical realism (Dassault Systèmes, 2022).

In the shear direction, the interaction is described by the advanced hypoplastic contact model detailed in Section 2. Unlike the soil continuum, which includes the Intergranular Strain (IGS) extension (Niemunis and Herle, 1997), the interface uses the basic hypoplastic formulation (von Wolffersdorff, 1996). This approach shares the soil's fundamental parameters but omits IGS variables, preserving pressure- and density-dependent friction with reduced computational cost. To ensure physical consistency, the interface elements are explicitly initialised with the same void ratio (e_0) and relative density (I_D) as the adjacent continuum elements, ensuring that pyknotropic effects are correctly inherited from the surrounding soil state. The model's behaviour is primarily governed by the interface roughness parameter κ, which represents the ratio of the maximum mobilised critical-state interface friction angle (δ_{cs}) to the soil's critical-state internal friction angle (φ_{cs}). The determination of κ is a critical step for an accurate simulation. While this parameter can be estimated from the literature or

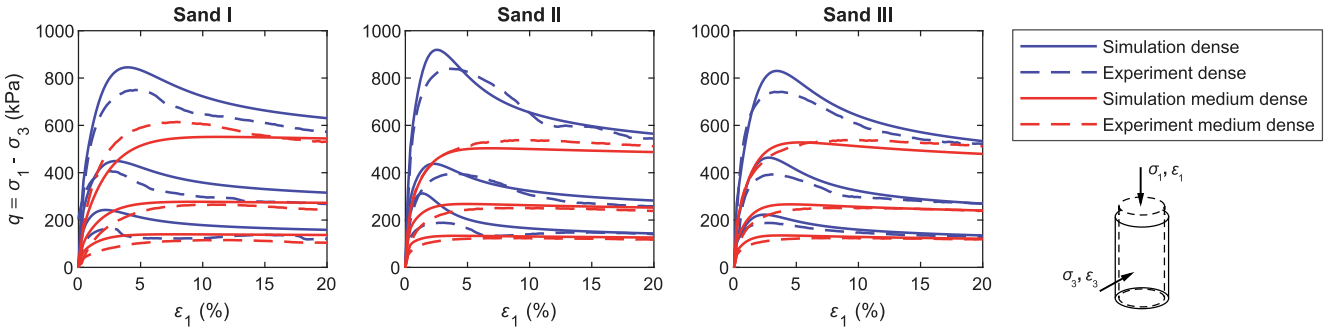

Fig. 4. Numerical simulations of CD triaxial tests on three different sand types Sand I (left), II (centre), and III (right) under various stress conditions (σ_3 = 50, 100, and 200 kPa) and relative densities (medium dense with $I_D \approx 0.55$ and very dense with $I_D \approx 0.95 - 1.0$).

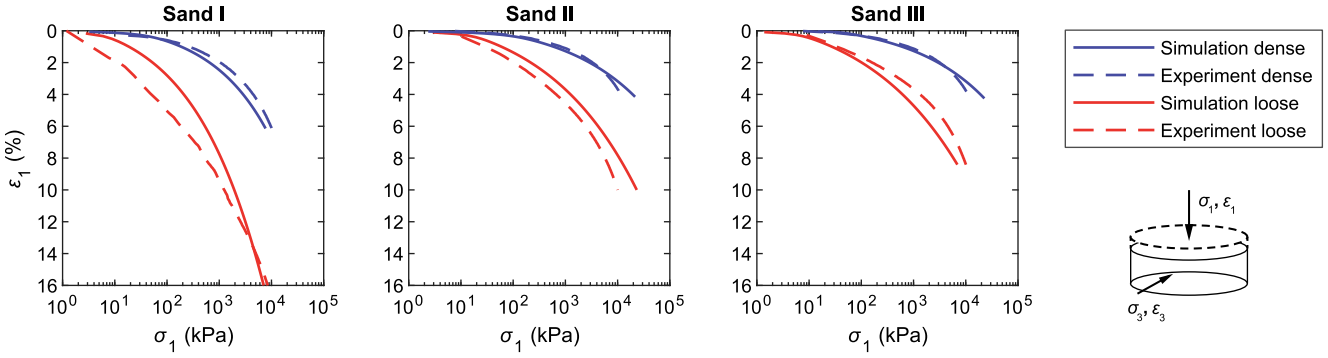

Fig. 5. Numerical simulations of CRS oedometric tests on three different sand types Sand I (left), II (centre), and III (right), conducted at two relative densities: loose ($I_D \approx 0.3$) and very dense ($I_D \approx 0.9 - 0.95$).

established design recommendations (e.g., EAU 2020, 2023; EA-Pfähle, 2013) when such data are unavailable, the most rigorous approach is to derive it directly from project-specific experiments.

For the cohesive layers, simpler models were employed, given their secondary role in the overall capacity. In the organic peat layer, a standard Coulomb friction model was used with a reduced friction coefficient of $\mu = \tan(1/3\varphi')$, accounting for the lower friction mobilisation due to organic fibres (Canakci et al., 2016; Ampera and Aydogmus, 2005; Alkateeb and Grabe, 2026). In the thin silt layers (in Layers 6 and 8), shaft friction was not considered due to their negligible load-bearing capacity.

Finally, the virtual shear zone thickness d_s, another key parameter of the hypoplastic contact model, was set to $20\,d_{50}$ for the sandy layers. This value, supported by literature (Teichmann, 1989; Tejchman and Wu, 1995; Maier, 2002; Arnold and Herle, 2006), offers an effective balance between physical representation and numerical efficiency. Since the interface is rough ($\kappa \approx 0.7$), a thicker shear band is physically engaged compared to a smooth interface. Therefore, the upper bound of the literature range ($20\,d_{50}$) was selected. While the selection of d_s carries some uncertainty, this challenge is comparable to determining other empirical parameters, such as the tangential penalty factor or relative tangential displacement required in Coulomb friction models, as implemented in software like Abaqus (Dassault Systèmes, 2022). An alternative to relying on literature ranges is to derive d_s by back-analysing interface shear tests via curve-fitting (Arnold and Herle, 2006; Arnold, 2008). For this study, however, a value derived directly from the literature was preferred. This approach offers a more forward determination that is not reliant on detailed experimental data for curve-fitting, which aligns well with the goal of predictive modelling. While d_s is chosen from literature ranges here, its influence is rigorously quantified in Section 5.3 to ensure that this assumption does not bias the primary findings.

4.5. Experimental calibration of the interface roughness parameter

To determine the key interface parameter κ, a calibration procedure was performed based on the results of laboratory interface shear tests, ensuring its physical basis before application in the full-scale pile simulation. In Arnold and Herle (2006), δ_{max} represents the maximally mobilised interface friction during shearing, whereas the present work uses the large-displacement (critical-state) plateau value δ_{cs}. This distinction is important because peak mobilisation is more sensitive to density and stress level, while the critical-state measure provides a more transferable reference for κ. It is emphasised that this calibration is performed independently of the pile load test results, distinguishing this study from a back-fitting exercise and ensuring the methodology remains predictive. The strategy involves a combined experimental-numerical approach using a torsional interface shear tester (IST), chosen for its ability to apply large, continuous shear displacements and avoid the stress concentrations inherent in conventional direct shear devices.

4.5.1. Experimental setup and methodology

A series of interface shear tests was performed using a GDS Instruments torsional interface shear tester (IST), illustrated in Fig. 6. For the tests, steel plates cut from the actual installed piles ($R_{max} \approx 20$ μm) were attached to the device's top cap to represent the in-situ condition. Circular soil samples with a radius of $r = 35$ mm were then prepared using the three test sands (I, II, and III), which were placed in five layers and compacted to a medium relative density of $I_D = 0.60$, with layer-wise compaction verified using mass-volume checks. Each sample was first consolidated under a target normal stress of 50, 100, or 200 kPa. Each test was conducted three times. The shearing phase was executed by rotating the lower platform at a constant rate of 1.637 °/min (equivalent to 0.5 mm/min linear displacement evaluated at the mean radius (r_m=r/2)), corresponding to an equivalent shear path of approximately 10 mm (Eq. (15)). The average interface shear

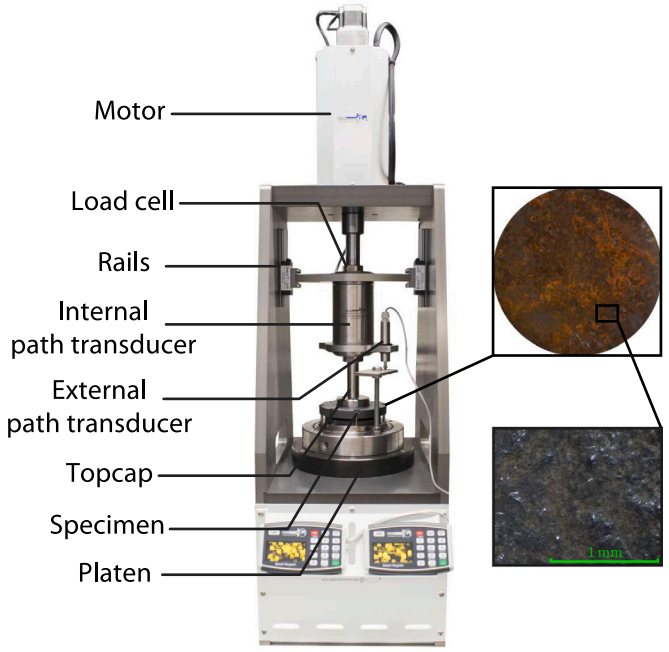

Fig. 6. Setup of the Interface Shear Tester from GDS Instruments with detailed images of the used steel surface.

stress τ was calculated from the measured torque M_T using Eq. (16) proposed by Yang et al. (2008):

$$s = \theta \cdot \frac{r \cdot \pi}{360} . \tag{15}$$

$$\tau = \frac{3 \cdot M_T}{2\pi \cdot r^3} . \tag{16}$$

4.5.2. Numerical model of the interface shear test

A full three-dimensional finite element model was developed to accurately capture the torsional stress state. A 3D analysis was necessary because torsional shearing induces shear strains that vary linearly with radius ($s = \theta \cdot r$), a kinematic condition that cannot be accurately represented using standard 2D plane strain or axisymmetric simplifications. The numerical setup for simulating the torsional shear tests was implemented in Abaqus/Standard 2023, replicating the geometry of the experiment as illustrated in Fig. 7. The soil was discretised using C3D8R continuum elements with the hypoplastic material law, while the steel plate was modelled as a rigid body. The interaction between them was defined using the hypoplastic contact formulation. Boundary conditions were set to mirror the experiment: radial displacement was prevented, and the base was fixed. A geostatic step first established the target normal stress (σ_n) on the rigid plate. Subsequently, a prescribed rotation was applied to the plate to shear the interface, replicating the experimental loading path.

4.5.3. Calibration procedure

The roughness parameter κ is determined using a systematic procedure that integrates the experimental and numerical results, as illustrated in the workflow in Fig. 8.

1. The critical-state interface friction angle δ_{cs} is calculated from the shear-to-normal stress ratio (τ_{cs}/σ_n) observed in the physical experiments, averaged over three replicates for each sand type.
2. The soil's internal friction angle φ_{cs} is determined numerically by simulating the IST with the exact 3D geometry and boundary conditions of the apparatus using a perfectly rough interface ($\kappa = 1.0$). This forces the shear plane to develop entirely within the soil continuum, yielding the soil's internal friction angle under the specific stress and boundary conditions of the test apparatus.
3. The roughness parameter is then calculated for each sand type as $\kappa = \delta_{cs}/\varphi_{cs}$.

This integrated approach provides a consistent basis for determining κ, as the numerically derived φ_{cs} represents the soil's strength under the specific stress and boundary conditions imposed by the IST apparatus, ensuring a direct correspondence between the experimental and numerical frameworks. This process yielded distinct values for each soil type, as detailed in Table 6.

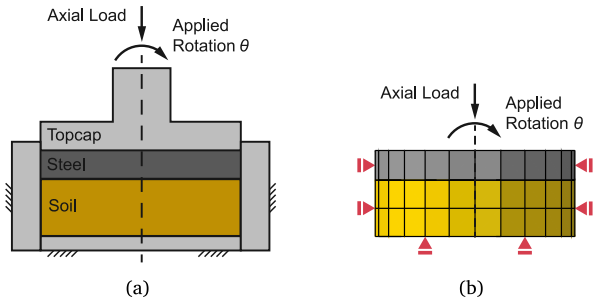

Fig. 7. Schematics of the torsional interface shear test. (a) Experimental setup showing the steel plate and soil sample under axial load and rotation (θ). (b) The equivalent numerical model illustrating the mesh, boundary conditions, and applied loads.

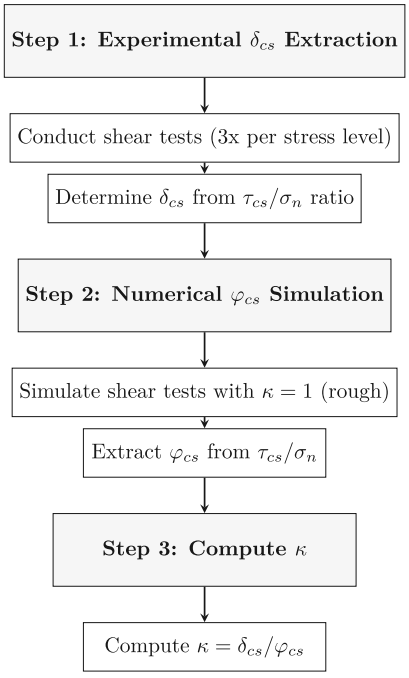

Fig. 8. Flowchart of the combined experimental-numerical methodology used to calibrate the interface roughness parameter κ.

Table 6
Summary of the calibrated interface roughness parameter (κ) derived from experimental (δ_{cs}) and numerical (φ_{cs}) friction angles for each sand type.

	δ_{cs} (°)	φ_{cs} (°)	$\kappa = \delta_{cs}/\varphi_{cs}$ (–)
Sand I	26.00	33.00	0.78
Sand II	22.32	32.79	0.68
Sand III	21.80	33.05	0.66

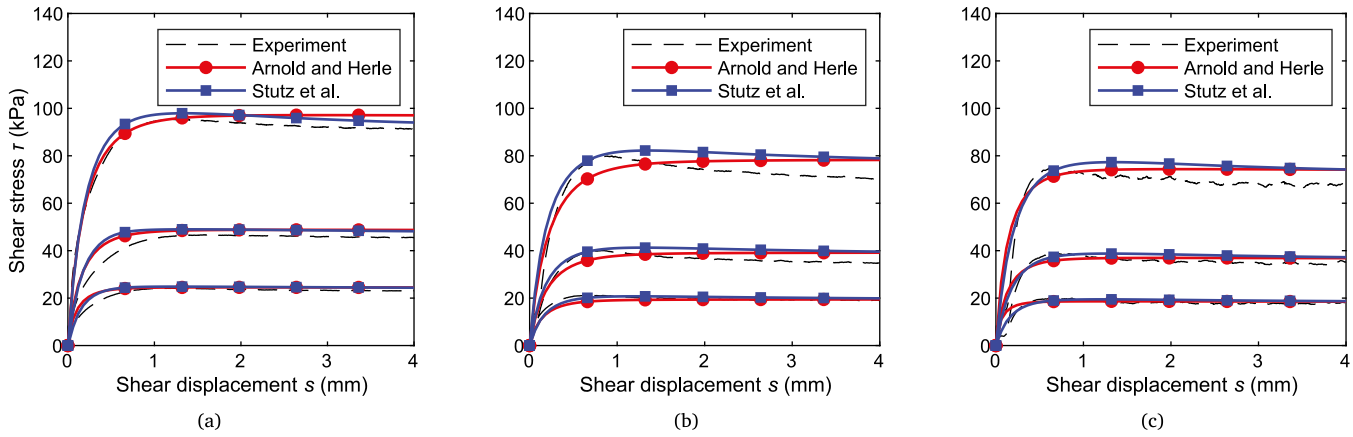

Fig. 9. Comparison of numerical simulations using the Arnold and Herle (2006) and the enhanced Stutz et al. (2016) hypoplastic contact model formulations against experimental torsional shear test results for (a) Sand I, (b) Sand II, and (c) Sand III under varying normal stresses (σ_n = 50, 100, and 200 kPa).

While the combined experimental-numerical calibration provides a robust method for determining κ, alternative approaches exist that rely on empirical correlations or established design guidelines. For instance, Subba Rao et al. (1998) proposed estimating the interface friction ratio based on relative roughness, defined as the ratio of average surface roughness to weighted average particle size. Similarly, Lings and Dietz (2005) and Gutjahr (2003) developed frameworks relating the roughness parameter to normalised roughness ($R_n = R_{\max}/d_{50}$), accounting for the interplay between surface texture and grain size. Furthermore, established design codes (Brumund and Leonards, 1973; U.S. Army Corps of Engineers, 1991; EAU 2020, 2023; EA-Pfähle, 2013; DIN 4085:2017-08, 2017) often recommend a constant ratio of $\delta/\varphi \approx 2/3$ for rough steel-sand interfaces, interpreted here as $\delta_{cs}/\varphi_{cs} \approx 2/3$. It is notable that the average of the experimentally calibrated values in this study ($\kappa \approx 0.67$) aligns well with these standard recommendations, providing mutual consistency between the advanced experimental procedure and established engineering practice.

Table 6 presents the experimentally calibrated κ values for the three sand types. A divergence is observed for the fine Sand I, where the experimental calibration yielded a higher value ($\kappa = 0.78$). This suggests that for the corroded steel surface ($R_{\max} \approx 20$ μm), the interface behaviour was in a "fully rough" regime relative to the fine grain size. However, for the dominant load-bearing layers (Sand II and III), the calibrated values ($\kappa \approx 0.66$–0.68) align closely with standard recommendations.

4.5.4. Results and selection of the hypoplastic contact formulation

The numerical performance using the calibrated parameters is validated against the experimental torsional shear data in Fig. 9. The simulations exhibit strong agreement with the laboratory measurements across all sand types and normal stress levels, accurately capturing the non-linear mobilisation and subsequent evolution of interface shear stress. A quantitative assessment yields a mean absolute percentage error (MAPE) below 9.4% for all test combinations, confirming the suitability of the hypoplastic contact framework and the calibrated parameters listed in Table 6 for this application.

To select the optimal hypoplastic contact formulation for the full-scale analysis, the standard model by Arnold and Herle (2006) and the enhanced formulation by Stutz et al. (2016) were benchmarked. As illustrated in Fig. 9, both formulations produce nearly identical load–displacement responses under the monotonic torsional loading conditions considered here. While the model by Stutz et al. (2016) predicted marginally higher peak shear stresses in some instances, aligning slightly better with experiments, the differences in pre-peak stiffness and residual strength were negligible. Both formulations demonstrated strong agreement with experimental measurements.

Preliminary full-scale pile simulations benchmarked both contact formulations. While the enhanced formulation by Stutz et al. (2016) offers theoretical advantages for general stress states, the formulation by Arnold and Herle (2006) proved more numerically stable for this boundary value problem, particularly during the sharp unloading–reloading transitions. Both formulations produced essentially equivalent global load–displacement responses; however, the enhanced formulation required substantially smaller time increments (often $< 10^{-4}$ s) and exhibited more frequent local convergence difficulties, resulting in a significantly higher computational cost without measurable improvements in predictive accuracy. Consequently, the formulation by Arnold and Herle (2006) was adopted for the full-scale analyses to ensure stable convergence while preserving the accuracy of the global load–displacement prediction. It is acknowledged, however, that for more complex loading paths involving pronounced stress rotations and/or cyclic loading, the enhanced formulation by Stutz et al. (2016) would be theoretically preferable.

5. Results and discussion

This section details the numerical results. The main analysis benchmarks the hypoplastic and Coulomb models against the full-scale field tests. This comparison is supported by mesh convergence and parametric sensitivity studies that confirm the model's stability and explore the influence of key parameters.

5.1. Comparison of contact models: hypoplastic vs. coulomb friction model

Fig. 10 presents a comparison of measured and simulated load–displacement curves, employing both hypoplastic and Coulomb contact laws. The results are presented in two complementary formats: a linear representation on the left and a logarithmic scale on the right. This dual approach highlights early-stage stiffness discrepancies between pile displacement and applied load. The linear representation also includes an enlarged section detailing initial displacements up to 8 mm, effectively illustrating the accurate capture of the initial load-bearing behaviour. The experimental data reveal a characteristic pattern: an approximately linear increase in pile resistance up to about 400 kN, followed by unloading and reloading phases. This is followed by pronounced non-linear behaviour, characterised by a gradual reduction in stiffness until reaching a maximum tensile capacity of approximately 600 kN.

The hypoplastic contact model exhibits substantially improved agreement with the measured field response across the entire loading history. It effectively captures not only the ultimate load capacity but also critical features of the pre-failure response, including initial stiffness and a realistic representation of the unloading–reloading

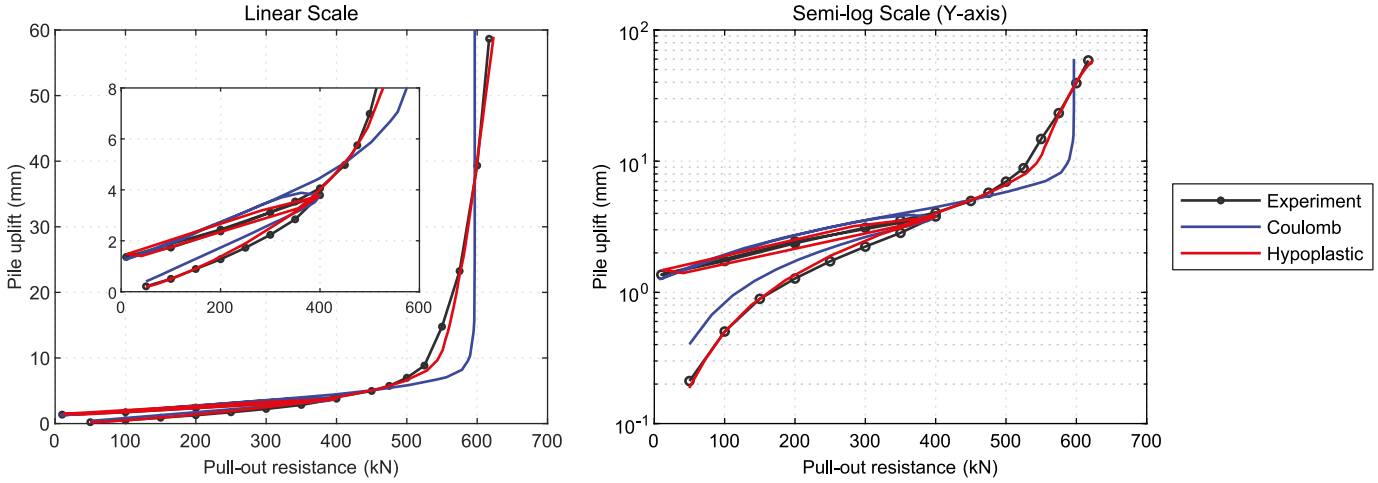

Fig. 10. Comparison of load–displacement curves from experimental measurements with numerical calculations using the hypoplastic and Coulomb contact models: (left) linear representation with an enlarged view of the initial response up to 8 mm, and (right) logarithmic representation of pile displacement, which emphasises the behaviour at small displacements and the beginning of the non-linear response.

Table 7
Prediction error (MAPE and RMSE) for the Coulomb and hypoplastic contact models across the loading, unloading, and reloading phases.

Phase	Coulomb model		Hypoplastic model	
	MAPE (%)	RMSE (kN)	MAPE (%)	RMSE (kN)
Loading	24.20	51.52	14.50	14.51
Unloading	44.34	34.62	16.70	26.95
Reloading	5.03	28.54	1.30	7.74
Weighted avg.	7.67	30.14	2.64	8.83

cycle. This accuracy stems from the model's formulation, which inherently considers the material's stress history and its non-linear, state-dependent stiffness. Quantitatively, the weighted-average mean absolute percentage error (MAPE) is 2.64% and the root mean square error (RMSE) is 8.83 kN, representing a 71% reduction relative to the Coulomb model (RMSE 30.14 kN). Table 7 summarises the error metrics. The "Weighted avg". error E_w is calculated by weighting the error from each phase E_p using a weight w_p that is proportional to its pile-head uplift span $\Delta u_p^{\text{overlap}}$:

$$w_p = \frac{\Delta u_p^{\text{overlap}}}{\sum_q \Delta u_q^{\text{overlap}}}, \qquad E_w = \sum_p w_p E_p, \tag{17}$$

where E denotes either MAPE or RMSE, and $\Delta u_p^{\text{overlap}} = \max(u)_p - \min(u)_p$ over the common data range. This method gives greater significance to phases with larger deformations.

In contrast, the simpler Coulomb contact model shows significant deviations. The initial stiffness is notably underestimated. During the unloading phase, the load decreases with a slope nearly identical to that during loading, while the experimental data show a particularly steeper decline, indicating a more pronounced degradation of shaft resistance. This model exhibits typical linear-elastic, perfectly plastic behaviour, with an abrupt transition to the plastic region at failure. The results emphasise the substantial influence of the contact model on the simulation outcomes. Although the hypoplastic model is used for the continuum, the Coulomb friction model fails to capture many essential aspects of interface behaviour, resulting in an inadequate representation of the complex pile-soil interaction, reflected in an increased weighted average MAPE of 7.67%. It is worth noting, however, that the simpler Coulomb model provided a reasonable prediction of the local strain distribution in the previous Class-A simulations (Alkateeb and Grabe, 2026).

However, the enhanced accuracy of the hypoplastic contact model comes at the cost of increased computational requirements. For the analyses presented, simulations were conducted on a system equipped with an AMD Ryzen Threadripper 7960X 24-core processor (4.20 GHz) and 64.0 GB of RAM, utilising eight cores for parallel processing. On this system, the simulation using the Coulomb contact model required 37 iterations and a total time of approximately 570 s. In contrast, the hypoplastic contact model required 134 iterations and approximately 3480 s. This represents approximately a six-fold increase in computational cost, which is primarily attributable to the more complex, state-dependent constitutive updates and the associated increase in global iterations. For single-pile design in complex stratified profiles, this additional expense is justified by the significant 71% reduction in prediction error, particularly for high-stakes projects where the consequences of capacity uncertainty are severe. However, for larger-scale applications (e. g., pile groups), where computational demands scale considerably, practical adoption may require acceleration strategies. Future implementations could benefit from reduced-order modelling, selective mesh coarsening in regions remote from the pile-soil interface, sub-structuring techniques, or selective domain discretisation, restricting the computationally intensive hypoplastic formulation to the mechanically decisive interface zones while employing simpler constitutive laws in the far-field (Bathe, 2006; Boulbes, 2020). Therefore, the decision to use the more computationally intensive hypoplastic model should be carefully considered in relation to the importance of achieving higher predictive accuracy for a particular engineering application.

These results demonstrate that a more comprehensive and accurate representation of pile behaviour under axial tensile loading is achieved by employing a high-quality hypoplastic contact model, marking a notable advancement in geotechnical modelling.

5.2. Mesh convergence & computational cost

To investigate the influence of mesh refinement on the calculated load–displacement behaviour of the tension pile, a systematic variation of the finite element mesh was performed. Three different discretisation levels were considered: a coarse mesh with 35,170 elements, a medium mesh with 74,488 elements, and a fine mesh with 174,224 elements, as shown in Fig. 11. The results in Fig. 12 show that even the coarse mesh provides satisfactory agreement with the experimental data. For small displacements up to about 6 mm, all three mesh variants show nearly identical results. At larger displacements, minor deviations occur, with the fine mesh providing the best representation of the experimental

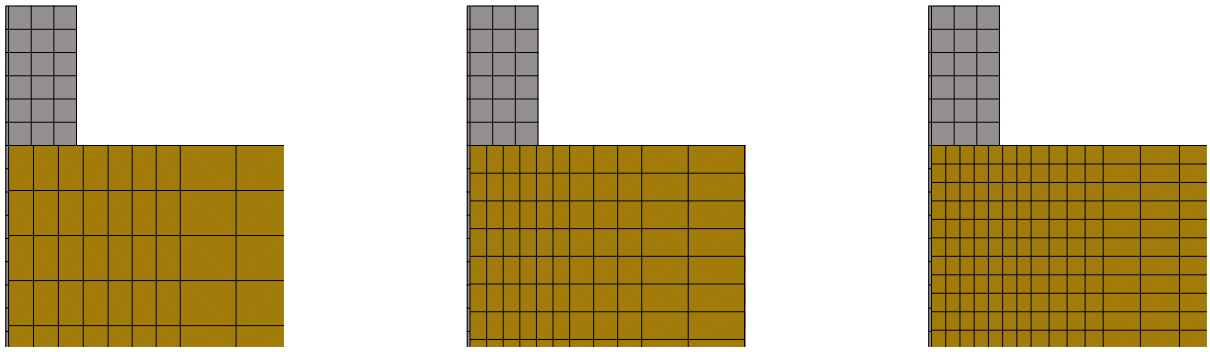

Fig. 11. Comparison of FE mesh refinements used for numerical calculations: coarse mesh (35,170 elements, a), medium mesh (74,488 elements, b), and fine mesh (174,224 elements, c).

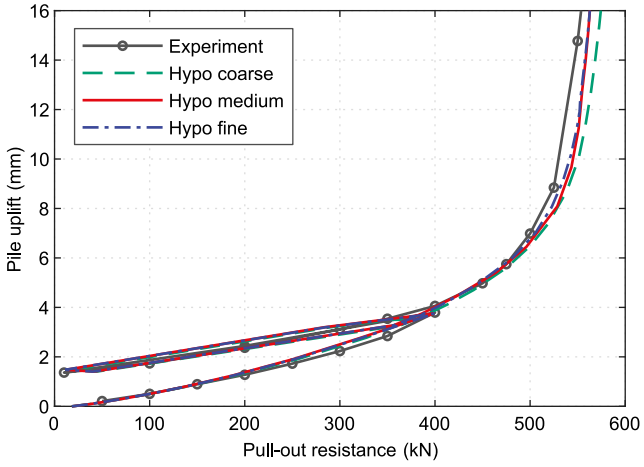

Fig. 12. Influence of FE mesh refinement on the load–displacement behaviour of the tension pile: Comparison between experimental data and numerical simulations with different numbers of elements (35,170, 74,488, and 174,224 elements).

data. For clearer visualisation of the initial stiffness and the load–unload–reload cycles, the pile head displacement axis in Fig. 12 is limited to 16 mm.

The quantitative analysis presented in Table 8 reports the MAPE and RMSE of the coarse and medium meshes relative to the fine-mesh solution, which is treated as the numerical reference. The pointwise errors were evaluated at matched pile-head displacements, using interpolation where required. The coarse mesh (35,170 elements) required a computation time of 1033 s and yields a weighted-average MAPE of 2.64% and RMSE of 8.25 kN with respect to the fine mesh. The medium mesh (74,488 elements) improves the agreement substantially (weighted-average MAPE 0.46% and RMSE 2.32 kN) at a computation time of 3480 s. Further refinement to the fine mesh provides only marginal additional changes in the global load–displacement response compared to the increased computational effort (6259 s). Based on this trade-off, the medium mesh was selected as the optimal compromise between accuracy and efficiency for all subsequent analyses, and the results confirm numerical convergence of the solution with respect to mesh refinement.

5.3. Parametric sensitivity analysis

Several key geotechnical and interface parameters can influence the predictive accuracy and behaviour of the numerical model. To assess these effects within the hypoplastic framework, a systematic parametric sensitivity analysis was conducted. This involves varying the pile surface roughness (κ), the soil relative density, the virtual shear zone thickness (d_s), the in-situ earth pressure coefficient (K_0) and the pile circumference U_{profile} from their baseline values used in the main back-analysis. The following paragraphs detail the investigation and impact of each of these parameters on the predicted pile pull-out response.

Table 8
Performance of hypoplastic model mesh variants (coarse vs. medium) across load phases.

Phase	Hypoplastic coarse		Hypoplastic medium	
	MAPE (%)	RMSE (kN)	MAPE (%)	RMSE (kN)
Loading	2.08	4.40	1.37	3.36
Unloading	6.87	7.28	0.63	1.09
Reloading	2.51	8.52	0.40	2.30
Weighted avg.	2.63	8.25	0.46	2.32

Influence of pile surface roughness (κ)

The surface roughness of the pile plays a crucial role in the mobilisation of shaft friction. The numerical investigations conducted with the hypoplastic contact model show a clear dependence of the load–displacement behaviour on the roughness parameter κ. For the analysis, three different roughnesses were investigated: $\kappa = 0.40$ (smooth), $\kappa = 0.67$ (calibrated baseline), and $\kappa = 0.85$ (rough).

The simulation results in Fig. 13 illustrate a clear, monotonic dependence of the pull-out response on the roughness parameter. Both the initial stiffness and the overall tensile capacity increase with higher κ values. At a pile displacement of 3 mm, the rough surface already achieves a pile resistance of about 450 kN, while the smooth surface mobilises only about 250 kN.

The simulation employing the calibrated value of $\kappa \approx 0.67$ demonstrates the best agreement with the experimental data across the entire loading and unloading–reloading history. This aligns with the average of the experimentally calibrated values (Table 6) and confirms its suitability as a representative parameter. The smooth interface ($\kappa = 0.40$) underestimates the pile resistance and exhibits more pronounced post-peak softening. Conversely, the rough case ($\kappa = 0.85$) yields an overly stiff response that forms an upper-bound envelope to the measured behaviour and shows a more gradual decrease in resistance after the peak. This behaviour is consistent with the physical mechanisms represented in the hypoplastic contact model. A higher roughness corresponds to stronger interlocking between the soil and the pile surface, which sustains shear resistance more effectively at larger displacements. Furthermore, since κ directly scales the admissible shear stress for a given normal stress, its influence is amplified with depth due to

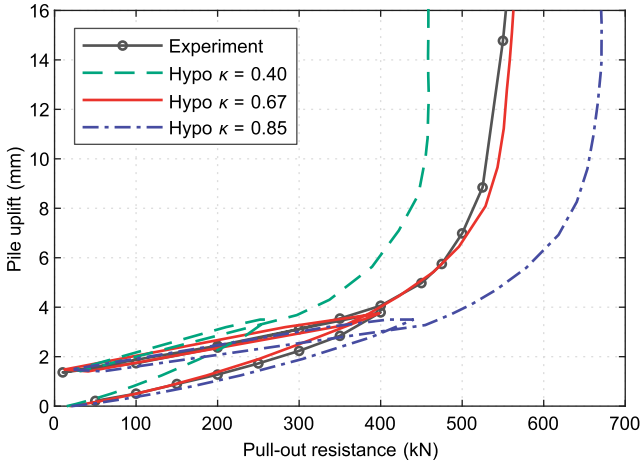

Fig. 13. Influence of the friction parameter κ on the load–displacement behaviour of the tension pile: comparison of numerical simulations with different κ values against the experimental data.

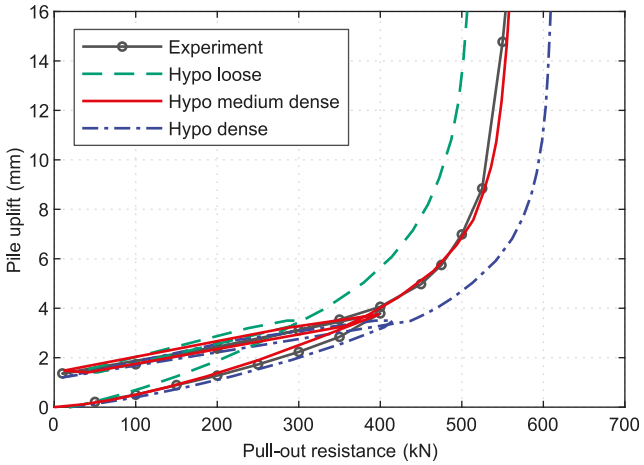

Fig. 14. Influence of relative density (I_D) on load–displacement behaviour. The plot compares experimental data with simulations using the realistic CPT-derived profile ($I_{D,avg} \approx 0.64$) and two simplified uniform states: dense ($I_D = 0.84$) and loose ($I_D = 0.30$).

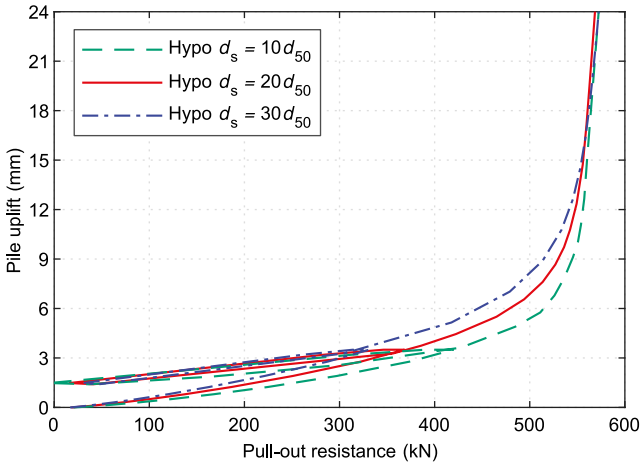

Fig. 15. Influence of virtual shear zone thickness (d_s) on the load–displacement behaviour of the tension pile.

the model's inherent consideration of barotropy (pressure dependency). This analysis underscores that an accurate characterisation of interface roughness is essential for a reliable prediction of the pile's load-bearing behaviour.

Effects of soil relative density (I_D)

The initial compaction state of the soil, represented by its relative density (I_D), is a critical parameter governing the pile's load–displacement response. For the main analysis, a realistic initial state was established using a depth-dependent I_D profile derived from in-situ CPT data (as detailed in Section 4.3). This profile corresponds to a medium-dense to dense state, with a thickness-weighted average of $I_D \approx 0.64$. To investigate the model's sensitivity to this parameter, the simulation based on the realistic CPT-derived profile was compared against two simulations using simplified, uniform density assumptions. These comparative cases represented a globally loose state, with a uniform $I_D = 0.30$ applied to all sand layers, and a globally dense state, with a uniform $I_D = 0.84$.

The numerical results are compared against the experimental data in Fig. 14. The simulation using the CPT-derived profile ($I_{D,avg} \approx 0.64$) provides the best agreement with the measured field response. In contrast, the simplified uniform cases bound the realistic behaviour: the dense-state simulation shows significantly higher stiffness, while the loose-state simulation substantially underestimates both stiffness and capacity. At a displacement of 15 mm, the difference in pile resistance between the uniform dense and loose states is about 100 kN. These results confirm the model's high sensitivity to the initial soil state and emphasise the importance of accurately determining the in-situ relative density profile for a realistic and reliable prediction of pile load-bearing behaviour.

Effect of virtual shear zone thickness (d_s)

The virtual shear zone thickness d_s is a parameter in the hypoplastic contact model representing the nominal thickness of the shearing soil layer adjacent to the pile surface. As discussed in Section 4.4, a value of $d_s = 20\,d_{50}$ was adopted for the primary analyses, based on literature and a balance between physical representation and numerical efficiency.

To assess the model's sensitivity to this parameter, additional simulations were performed with d_s values of $10\,d_{50}$ and $30\,d_{50}$. Fig. 15 illustrates the load–displacement curves for these different d_s values. The results indicate that variations in d_s within this investigated range have a discernible but not dominant effect on the predicted pull-out response. A smaller d_s value implies that a given relative pile-soil displacement translates into a larger shear strain within the interface element, which can lead to a slightly faster mobilisation of shear stress. Conversely, a larger d_s may lead to a more ductile response.

The selection of d_s introduces a degree of uncertainty, a challenge common to many advanced contact models. For instance, conventional Coulomb friction models require a similar empirical estimation for the critical elastic slip. However, the sensitivity analysis presented here is crucial for contextualising this uncertainty. While variations in d_s produce discernible changes in the response (Fig. 15), their influence is demonstrably secondary when compared to the effect of core physical parameters like relative density I_D (Fig. 14) and interface roughness κ (Fig. 13). This finding confirms that the numerical framework is reliable and that the primary conclusions of the study are not controlled by the specific choice of d_s within its physically reasonable range.

Sensitivity to in-situ earth pressure coefficient (K_0)

The initial horizontal effective stress state in the ground, characterised by the coefficient of earth pressure at rest (K_0), significantly impacts the normal stresses acting on the pile shaft, and consequently,

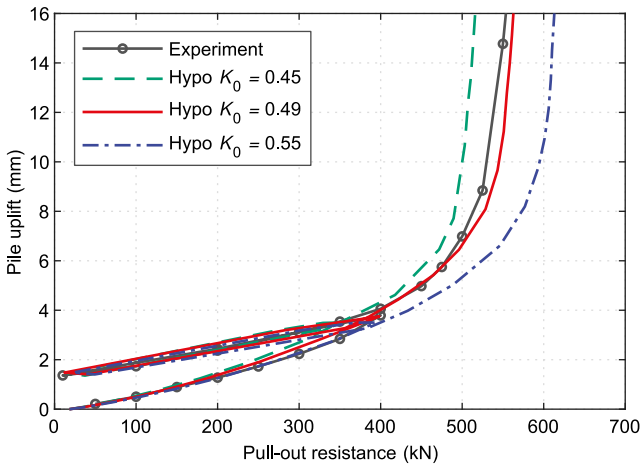

Fig. 16. Influence of the earth pressure coefficient K_0 on the load–displacement behaviour of the tension pile: Comparison between experimental data and numerical simulations with K_0 = 0.45, K_0 = 0.49, and K_0 = 0.55.

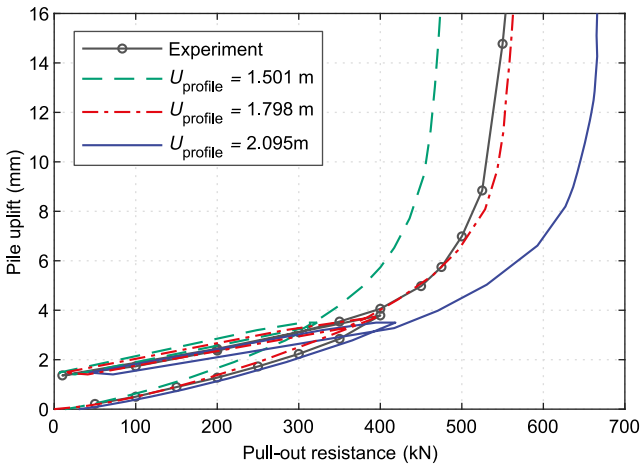

Fig. 17. Influence of pile circumference ($U_{profile}$) on the load–displacement behaviour. The plot compares experimental data with numerical simulations for three different profile circumferences, with the baseline case representing the actual pile ($U_{profile}$ = 1.798 m).

the mobilised shaft friction. A sensitivity analysis was conducted by systematically varying K_0 values. These included 0.45, a baseline of 0.49, and 0.55, covering a typical range for medium-dense sands (Ziccarelli, 2024). The baseline K_0 value of 0.49 corresponds to the thickness-weighted average of the K_0 values used in the individual sand layers (calculated via Jaky's formula $1 - \sin\varphi'$ as described in Section 4.2).

The results are shown in Fig. 16. In the initial loading phase, for small pile displacements (up to approximately 4 mm), all three K_0 variants yield broadly similar load–displacement responses with only minor deviations. However, as displacements increase, the influence of K_0 becomes progressively more pronounced. The simulation with a lower K_0 value of 0.45 results in an earlier mobilisation of the peak pile resistance and systematically underestimates the experimentally measured capacity. Conversely, the higher K_0 value of 0.55 slightly increases capacity, as the larger horizontal stresses contribute to a stronger activation of shaft friction. The simulation using $K_0 = 1 - \sin\varphi'$ demonstrates the best overall agreement with the experimental data across the entire displacement range, supporting the applicability of Jaky's formula for estimating K_0 in this context.

At a displacement of about 15 mm, the difference in pile resistance between the extreme values (K_0 = 0.45 and K_0 = 0.55) is about 100 kN. This substantial deviation illustrates the high sensitivity of the numerical model to the chosen initial earth pressure coefficient.

Influence of pile circumference ($U_{profile}$)

The pile's circumference ($U_{profile}$) is a fundamental parameter governing tensile capacity. To quantify its effect, the circumference was varied from 1.501 m to 2.095 m, with the baseline of 1.798 m representing the as-built HP 320 x 88.5 pile.

The results in Fig. 17 confirm the expected direct relationship: a larger circumference yields a higher pull-out resistance. More importantly, the simulation using the actual geometric circumference shows good agreement with the experimental data, indicating that complex mechanisms, such as "soil plugging", were not a dominant mechanism. If significant plugging had occurred, the effective circumference would be closer to the box perimeter (significantly smaller than the actual coated area), leading to an overprediction of capacity when using the full perimeter. The close match using the full geometric perimeter suggests that plugging effects were minimal and shear resistance was mobilised along the entire steel surface area. However, extrapolating these findings to large-diameter monopiles requires caution, as differences in slenderness (L/D), installation stresses, and unique H-pile soil-flange interlock mean the quantitative results are not directly scalable.

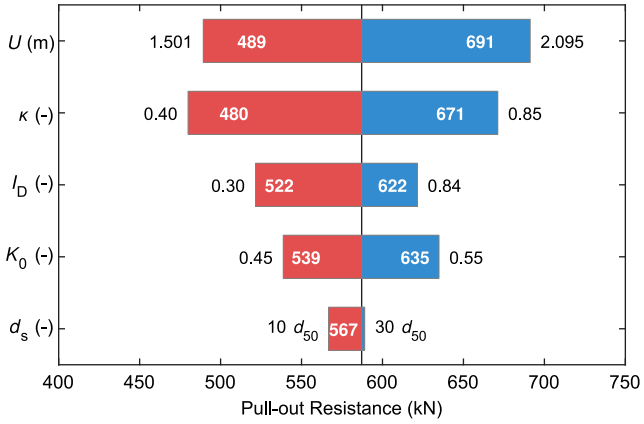

Fig. 18. Tornado plot summarising the sensitivity of the ultimate pile capacity (P_{ult}) to variations in key input parameters relative to the calibrated baseline value (P_{ult} = 600 kN). Note that the ranges differ for each parameter and represent the physically plausible uncertainty rather than a standardised variation.

Summary of parametric sensitivity

To synthesise the findings, a tornado plot (Fig. 18) was created. The plot visually ranks the design parameters by their impact on the ultimate pile capacity (P_{ult}) in comparison to the baseline result (P_{ult} = 600 kN) when each parameter is varied over its investigated range, as detailed in Table 9.

The analysis identifies the interface roughness (κ) and the pile circumference (U) as the most influential parameters, each capable of altering the ultimate capacity by approximately ±17–18%. This finding demonstrates that precise characterisation of surface roughness and careful selection of pile geometry are more critical for accurate capacity prediction than sophisticated soil constitutive modelling alone. Relative density (I_D) and the in-situ earth pressure coefficient (K_0) have moderate, yet still significant, influence (±8–11%), highlighting the importance of proper site investigation and stress state determination. The virtual shear zone thickness (d_s) has a negligible impact on the ultimate capacity, confirming the model's validity with respect to this numerical parameter. For engineering practice, these results emphasise that accurate capacity prediction depends primarily on realistic representation of physical interface conditions, guiding where to focus calibration and quality assurance efforts. Building on the parametric

Table 9
Overview of sensitivity analyses, showing the number of levels tested for each parameter. The reference baseline case is in bold.

Parameter	Unit	No. of levels	Investigated levels
Numerical & model choices			
Contact model	–	2	Coulomb, **hypoplastic**
Mesh discretisation	–	3	Coarse, **medium**, fine
Geotechnical & interface parameters			
Relative density I_D	(–)	3	0.3 (loose), **0.64 (medium)**, 0.84 (dense)
Surface roughness κ	(–)	3	0.4 (smooth), **0.67 (rough)**, 0.85 (very rough)
Shear zone thickness d_s	(mm)	3	$10 \cdot d_{50}$, **$20 \cdot d_{50}$**, $30 \cdot d_{50}$
Earth pressure coeff. K_0	(–)	3	0.45, **0.49**, 0.55
Pile circumference $U_{profile}$	(m)	3	1.501, **1.798**, 2.095

study, a preliminary qualitative Buckingham-Π_P analysis formulates a simplified dimensionless relationship for ultimate pull-out capacity scaling trends: $\Pi_P \propto \kappa^{0.39} K_0^{0.78}$. Detailed derivation and limitations are in Appendix C.

5.4. Limitations of the present study

While this study successfully demonstrates the enhanced predictive capabilities of the 3D hypoplastic contact model, certain limitations contextualise the findings and guide future research.

The primary methodological limitation is the wished-in-place (WIP) approach, which neglects explicit simulation of installation effects such as soil displacement, densification, stress changes, and subsequent time-dependent set-up. Simulating the full installation process, comprising combined vibratory and impact driving followed by time-dependent consolidation, remains computationally prohibitive and methodologically challenging and represents a research frontier rather than the current state of practice (Alkateeb and Grabe, 2026). Consequently, the WIP assumption serves as a standard and pragmatic baseline in geotechnical numerical modelling. However, as discussed in Section 4.2, adopting the WIP approach with conservative K_0 assumptions establishes a valid lower-bound foundation, isolating the performance of the contact formulation from installation-related uncertainties. Future research could address this challenge by employing large-deformation numerical frameworks, such as the Coupled Eulerian-Lagrangian (CEL) (Benson, 1992) method or the Material Point Method (MPM) (Al-Kafaji, 2013), to explicitly simulate the penetration process and the resulting stress field alteration. To mitigate the high computational costs inherent in such explicit installation simulations, advanced acceleration techniques, such as Mass-Gravity-Scaling (MGS) (Kencana et al., 2021) or kinematic coupling of shell and volume elements (Osthoff and Grabe, 2018), could be integrated to render such comprehensive analyses computationally feasible.

Further idealisations were made in the material modelling. Cohesive soil layers (peat and silt) were represented with a simplified Mohr–Coulomb model, and soil parameters were assumed to be homogeneous within layers.

Finally, the scope of this work is a focused, mechanistic single-case assessment rather than a statistical validation across multiple sites or piles. Comparable public datasets featuring such complex conditions—with high-resolution instrumentation and detailed stratigraphic definition—are currently scarce; the Niederfinow test is exceptional in this regard. Extending the comparison to additional piles, loading histories, and installation modelling remains an important direction for future work once sufficiently complete datasets become available.

While these limitations are inherent to the current state of practice, they provide specific directions for future research. The quantified improvements demonstrated by the hypoplastic contact model remain valid within these acknowledged constraints.

5.5. Implications for geotechnical design practice

The computational cost of the hypoplastic contact model (approximately six times that of the Coulomb model in our study) necessitates clear guidelines for its application. The selection of the interface model should be driven by the governing design objective and by whether pile-soil interface behaviour controls the system response. The hypoplastic interface formulation is recommended when the analysis must accurately reproduce the non-linear load–displacement response beyond ultimate resistance, particularly regarding unloading–reloading stiffness, hysteretic damping, and state-dependent mobilisation in layered profiles. Conversely, the Coulomb interface remains appropriate for preliminary assessments and monotonic, capacity-focused checks in comparatively uniform ground conditions, where computational efficiency is prioritised. Accordingly, the hypoplastic interface should be employed when:

- Serviceability or displacement-based criteria govern the design, making the precise shape of the load–displacement curve (including unloading–reloading sequences) crucial.
- The soil profile exhibits strong stratification or thinly interlayering, leading to pronounced changes in stress paths along the shaft that simplified friction laws cannot capture.
- Interface behaviour is central to the design question, and a physically motivated calibration of roughness is feasible (e. g., based on interface shear testing or project-specific evidence).

In contrast, the Coulomb interface is sufficient when:

- The analysis is limited to homogeneous soil conditions or preliminary design phases where a monotonic estimate of ultimate capacity is adequate.
- The global system response is not primarily governed by complex interface phenomena.
- Computational resources are constrained, or very large-scale models are required, necessitating a low-cost baseline prior to verification-level refinements.

Regarding parameter determination, the interface roughness (κ) is identified as the most influential variable. Consequently, prioritising its experimental determination is essential. Where dedicated interface shear tests are unavailable, the standard recommendation from the literature for rough steel-sand interfaces provides a reasonable first estimate.

As for the allocation of site investigation resources, the sensitivity analysis (Fig. 18) indicates that the accuracy of the advanced model depends on the precise determination of physical state variables such as relative density (I_D) and interface roughness (κ). Obtaining high-resolution CPT data and performing interface shear tests should therefore take precedence over the refinement of numerical discretisation parameters such as the shear zone thickness (d_s).

6. Summary and outlook

This study presents the first detailed three-dimensional back-analysis of a hypoplastic contact model benchmarked against full-scale tensile load tests on driven steel piles in a highly stratified soil profile (23 layers), demonstrating that advanced interface formulations can be successfully implemented at field scale. The hypoplastic approach, calibrated using the same basic parameter set as the surrounding soil continuum, reproduces the main features of the non-linear and hysteretic pile-head response with a weighted mean absolute percentage error (MAPE) of 2.6%. Regarding the aggregated error measures, the hypoplastic interface reduces the weighted MAPE from 7.7% (Coulomb) to 2.6% and the total RMSE from 30.1 kN to 8.8 kN (an error reduction of approximately 66% and 71%, respectively) under the same continuum soil description. The results confirm that a holistic, physically realistic representation of the pull-out process requires that the contact model captures key soil–structure interaction phenomena, such as barotropy, pyknotropy, and the influence of surface roughness. In contrast, the Coulomb model proved incapable of replicating the observed field behaviour, even when the hypoplastic constitutive law describes the surrounding soil. A significant advantage of this implementation is that the hypoplastic contact model utilises the same constitutive parameters as the surrounding soil continuum, with the roughness parameter κ being the primary additional interface-specific value that requires estimation.

The calibration strategy directly links laboratory-scale interface characterisation to the full-scale simulation. The roughness parameter κ was derived from torsional interface shear tests, which represents the first numerical simulation of such tests using the hypoplastic contact model, using steel specimens cut from the actual piles and transferred to the full-scale field model without compensating back-fitting. For the governing sands (Sand II and Sand III), the calibrated values ($\kappa \approx 0.66$–0.68) are consistent with standard design guidance ($\delta/\varphi \approx 2/3$, interpreted here as $\delta_{cs}/\varphi_{cs} \approx 2/3$), indicating that literature-based initial estimates can be defensible but should be verified whenever interface behaviour controls serviceability or failure. The virtual shear zone thickness d_s is linked to grain size and was fixed accordingly (Section 4.3). This renders the advanced approach feasible in engineering practice, as it facilitates reliable Class-A predictions from routine laboratory data without the need for specialised field testing.

The parametric analyses confirm that interface roughness (κ) and pile circumference (U_{profile}) dominate the tensile capacity in the investigated configuration. Relative density (I_D) and the in-situ horizontal stress state (K_0) also exert a practically relevant influence because they control the normal stress level along the shaft and thereby the stress-dependent friction mobilisation. Variations in the assumed virtual shear zone thickness (d_s) affect the mobilisation rate but remain secondary within the investigated range, supporting the validity of the baseline assumption. For practical design, the computationally efficient Coulomb model is suitable for preliminary sizing and for cases where the design is governed by monotonic ultimate capacity in comparatively uniform ground. However, in layered profiles where displacement, unloading–reloading stiffness, or cyclic degradation controls the design, the hypoplastic contact model provides a physically motivated improvement that justifies the higher computational effort.

Further developments should address the current idealisations of the numerical framework. This includes incorporating installation-induced stress changes and set-up, extending the assessment to cyclic or dynamic loading, and refining the constitutive description of cohesive interlayers. Moreover, the explicit treatment of spatial soil variability and continued investigation of dimensionless correlations could support the development of simplified design charts that retain the mechanistic insights of the advanced interface formulation.

CRediT authorship contribution statement

D. Alkateeb: Writing – review & editing, Writing – original draft, Visualization, Validation, Software, Methodology, Investigation, Data curation, Conceptualization. **J. Grabe:** Writing – review & editing, Supervision, Methodology, Funding acquisition, Conceptualization.

Declaration of competing interest

The authors declare the following financial interests/personal relationships which may be considered as potential competing interests: Juergen Grabe reports financial support was provided by Federal Waterways Engineering and Research Institute. If there are other authors, they declare that they have no known competing financial interests or personal relationships that could have appeared to influence the work reported in this paper.

Appendix A. Equations of the hypoplastic model with intergranular strain extension

The constitutive response of the non-cohesive soils is described by the hypoplastic model of von Wolffersdorff (1996) with the intergranular strain extension by Niemunis and Herle (1997).

The base model relates the objective stress rate $\overset{\circ}{\mathbf{T}}$ to the deformation rate tensor $\boldsymbol{D}$ via:

$$\overset{\circ}{\mathbf{T}} = \mathbf{L} : \boldsymbol{D} + \mathbf{N}\|\boldsymbol{D}\| \,. \tag{A.1}$$

The material response is controlled by the linear and non-linear components of stiffness $\mathbf{L}$ and $\mathbf{N}$, which are given by:

$$\mathbf{L} = f_b f_e \frac{1}{\operatorname{tr}(\hat{\mathbf{T}}\cdot\hat{\mathbf{T}})}\left(F_l^2\mathbf{I} + a_l^2\hat{\mathbf{T}}\hat{\mathbf{T}}\right), \tag{A.2}$$

$$\mathbf{N} = f_b f_e f_d \frac{F_l a_l}{\operatorname{tr}(\hat{\mathbf{T}}\cdot\hat{\mathbf{T}})}\left(\hat{\mathbf{T}} + \hat{\mathbf{T}}^*\right), \tag{A.3}$$

with $\hat{\mathbf{T}} = \frac{\mathbf{T}'}{\operatorname{tr}\mathbf{T}'}$ and $\hat{\mathbf{T}}^* = \hat{\mathbf{T}} - \frac{1}{3}\mathbf{I}$. The equations are functions of the Matsuoka-Nakai failure condition F_l and several scalar factors: a model parameter a_l, a barotropy (pressure dependency) factor f_b, and pyknotropy (density dependency) factors f_e and f_d. These factors are defined as:

$$a_l = \frac{\sqrt{3}\left(3-\sin(\varphi_c)\right)}{2\sqrt{2}\sin(\varphi_c)},\quad f_e = \left(\frac{e_c}{e}\right)^{\beta},\quad f_d = \left(\frac{e-e_d}{e_c-e_d}\right) \tag{A.4}$$

$$f_b = \frac{h_s}{n}\left(\frac{e_{i0}}{e_{c0}}\right)^{\beta}\frac{1+e_i}{e_i}\left(\frac{3p'}{h_s}\right)^{1-n}\cdot\left[3+a_l^2-a_l\sqrt{3}\left(\frac{e_{i0}-e_{d0}}{e_{c0}-e_{d0}}\right)^{\alpha}\right]^{-1}.$$

For a comprehensive derivation of all terms, readers are referred to the original work in von Wolffersdorff (1996).

The intergranular strain (IGS) extension is included to capture high stiffness at small strain amplitudes and introduces the tensor $\hat{\boldsymbol{\delta}}$ as an additional state variable. The stress rate is then computed from a modified stiffness tensor $\mathbf{E}$:

$$\overset{\circ}{\mathbf{T}} = \mathbf{E} : \boldsymbol{D} \,, \tag{A.5}$$

where $\mathbf{E}$ incorporates the influence of $\hat{\boldsymbol{\delta}}$:

$$\mathbf{E} = \left[\zeta^{\chi} m_T + (1-\zeta^{\chi}) m_R\right]\mathbf{L} + \begin{cases} \zeta^{\chi}\left(1-m_T\right)\mathbf{L} : \hat{\boldsymbol{\delta}}\hat{\boldsymbol{\delta}} + \zeta^{\chi}\mathbf{N}\hat{\boldsymbol{\delta}} & \text{for} \quad \hat{\boldsymbol{\delta}} : \boldsymbol{D} > 0 \\ \zeta^{\chi}\left(m_R - m_T\right)\mathbf{L} : \hat{\boldsymbol{\delta}}\hat{\boldsymbol{\delta}} & \text{for} \quad \hat{\boldsymbol{\delta}} : \boldsymbol{D} \le 0 \end{cases}. \tag{A.6}$$

Appendix B. Numerical implementation of the contact model

The numerical implementation of the hypoplastic contact model is detailed in Algorithm 1. To ensure numerical stability and accuracy when integrating the highly non-linear rate equations, an explicit forward-Euler scheme with adaptive sub-stepping is employed. For each increment passed from Abaqus, the total time step is divided into a

Algorithm 1: Explicit integration for the hypoplastic contact model by Arnold and Herle (2006)

Result: Updated interface shear stress $\mathbf{T}^{i+1}$ and state variables $\mathbf{k}^{i+1}$ (e.g., void ratio e)
Divide total increment Δt into n_{sub} sub-increments δt
for $j = 1, 2, \ldots, n_{sub}$ do
  Calculate strain rate tensor $\mathbf{D}^j$ from slip and pressure increments over δt
  Calculate hypoplastic factors (F, a, f_b, f_e, f_d) using current state $(\mathbf{T}^j, \mathbf{k}^j)$
  Solve for normal strain rate $\dot{\varepsilon}_n$ satisfying the normal stress boundary condition
  Calculate objective shear stress rate $\overset{\circ}{\mathbf{T}}{}^{j}$ using the hypoplastic rate equation (Eq. (8))
  Update shear stress $\mathbf{T}^{j+1} \leftarrow \mathbf{T}^j + \overset{\circ}{\mathbf{T}}{}^{j}\,\delta t$
  Update state variables $\mathbf{k}^{j+1} \leftarrow f(\mathbf{k}^j, \dot{\varepsilon}_n, \delta t)$
Save final updated shear stress $\mathbf{T}^{i+1} \leftarrow \mathbf{T}^{n_{\text{sub}}}$
Save final updated state variables $\mathbf{k}^{i+1} \leftarrow \mathbf{k}^{n_{\text{sub}}}$

Algorithm 2: Implicit implementation scheme for the hypoplastic contact model by Stutz et al. (2017)

Result: Updated interface shear stress $\mathbf{T}^{i+1}$, state variables $\mathbf{k}^{i+1}$ (including e, σ_p), and consistent Jacobian $\mathbf{J}^{i+1}$
Transform incremental slip $\mathbf{u}$ (over the current increment Δt) to engineering shear strain increments: $\gamma_x/2 \leftarrow \arctan(u_x/d_s)$; $\gamma_y/2 \leftarrow \arctan(u_y/d_s)$
Set the target normal contact stress rate $\dot{\sigma}_n^{\text{press}}$ from the global solver
Store the normal stress at the beginning of the increment: σ_n^i
Make an initial guess for the normal strain rate $\dot{\varepsilon}_n^{(j=0)} \leftarrow 0$
for *Newton iterations* $j = 0, 1, \ldots$ do
  Assemble $\dot{\boldsymbol{\varepsilon}} = \left(\dot{\varepsilon}_n^{(j)}, 0, \dot{\gamma}_x/2, \dot{\gamma}_y/2\right)$ and call `UMAT`
  `UMAT` returns the updated normal stress σ_n^{UMAT} and the tangent Jacobian $\mathbf{C}^{tan}$
  Compute calculated normal stress rate: $\dot{\sigma}_n^{\text{UMAT}} \leftarrow (\sigma_n^{\text{UMAT}} - \sigma_n^i)/\Delta t$
  Compute error: err $\leftarrow \dot{\sigma}_n^{\text{press}} - \dot{\sigma}_n^{\text{UMAT}}$
  if $|err| \le TOL$ then
    break
  Update normal strain rate: $\dot{\varepsilon}_n^{(j+1)} \leftarrow \dot{\varepsilon}_n^{(j)} - f(\dot{\varepsilon}_n^{(j)})/f'(\dot{\varepsilon}_n^{(j)})$ using the error err
Update final interface stress $\mathbf{T}^{i+1}$ and Jacobian $\mathbf{J}^{i+1}$ by transforming the converged results from the `UMAT` back to `FRIC` format: $\sigma_n^{i+1} \leftarrow \sigma_n^{\text{UMAT}}$

series of smaller sub-steps. Within each sub-step, the interface strain rate tensor is calculated from the incremental slip and normal pressure provided by the main solver. The core hypoplastic constitutive law is then invoked to compute the objective rate of shear stress based on the current interface state. Finally, the interface shear stress and state variables, such as void ratio, are updated using a direct forward step. This procedure is realised in Abaqus by coupling the `FRIC` and `UMAT` user subroutines. The `FRIC` subroutine acts as a driver, translating the contact kinematics (slip and pressure) into stress and strain tensors. These tensors are then processed by the `UMAT` subroutine, which contains the full hypoplastic material logic. The more advanced formulation by Stutz et al. (2016) was implemented using an implicit update scheme, detailed in Algorithm 2. This method employs a local Newton–Raphson iterative loop within each time increment. This loop updates the normal strain rate $\dot{\varepsilon}_n$, until the calculated normal stress rate σ_n^{UMAT}, matches the normal stress rate prescribed by the global solver σ_n^{press}. This implicit approach ensures that the normal stress boundary condition at the interface is satisfied with high accuracy and provides a consistent tangent stiffness (Jacobian) matrix to the main solver, which typically enhances global convergence and allows for larger time steps.

Appendix C. Qualitative trend analysis of dimensionless scaling for pull-out capacity

This appendix outlines a preliminary investigation to develop a simplified, dimensionally consistent relationship for the ultimate pile pull-out capacity (P_{ult}). It is emphasised that the equation derived here represents a "qualitative trend analysis" derived from the numerical model to assist in preliminary design, rather than an empirical law derived from field data. It is not a validated empirical design formula and should not be used for direct design without project-specific verification.

C.1. Methodology and dataset

The analysis is based on a dataset of 20 unique, three-dimensional finite element method (FEM) simulations derived from the parametric study in Section 5.3. The capacity P_{ult} is defined as the load corresponding to a 30 mm pile head uplift, a criterion consistent with serviceability limits (EA-Pfähle, 2013). Key parameters were varied systematically across all sand layers using a one-factor-at-a-time (OFAT) approach. This method was chosen for its clarity in isolating the first-order influence of each parameter and for its computational efficiency, a significant consideration for complex, non-linear 3D FE models. The regression is based on an augmented subset of simulations derived from the parametric study. Compared to the main tornado-plot sensitivity (Fig. 18), additional intermediate levels were included. The parameters include: interface roughness (κ, 5 levels), relative density (I_{D}, 5 levels), virtual shear zone thickness (d_s/d_{50}, 3 levels), earth pressure coefficient (K_0, 5 levels), and pile circumference (U_{profile}, 6 levels). The pile embedment length (L) was held constant at 18.3 m.

C.2. Model formulation and trend analysis

Following the Buckingham Π theorem, a dimensionless pull-out capacity Π_P was formulated by normalising P_{ult} with a characteristic force representing the average effective stress acting on the pile shaft area:

$$\Pi_P = \frac{P_{\text{ult}}}{K_0 \cdot \gamma'_{\text{sands,avg}} \cdot (L/2) \cdot U_{\text{profile}} \cdot L}\,. \tag{C.1}$$

Here, $\gamma'_{\text{sands,avg}}$ is the thickness-weighted average effective unit weight of the sand layers, calculated for the global I_{D} state of each simulation. This dimensionless capacity was then related to the dimensionless predictors using a multiplicative power-law model:

$$\Pi_P = C \cdot \kappa^{\beta_1} \cdot I_{\text{D}}^{\beta_2} \cdot (d_s/d_{50})^{\beta_3} \cdot K_0^{\beta_4} \tag{C.2}$$

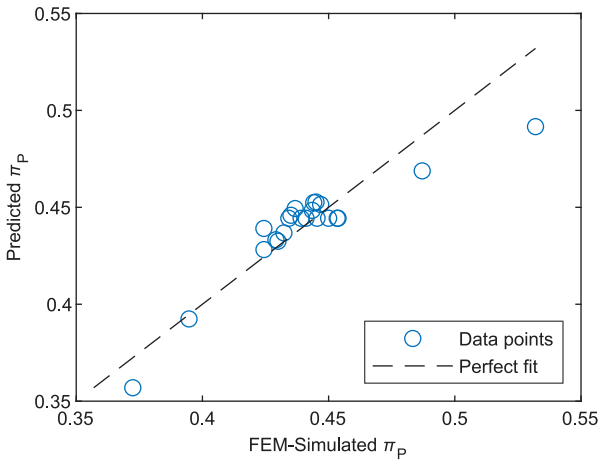

Fig. C.19. Performance of the dimensionless pull-out capacity model. The plot compares the FEM-simulated values of the dimensionless capacity Π_P against the values predicted by the regression model presented in Eq. (C.3). The dashed line indicates a perfect one-to-one fit.

Fitting the simulation data to this model (Fig. C.19) yielded the following relationship:

$$\Pi_P \approx 0.42 \cdot \kappa^{0.39} \cdot I_D^{0.053} \cdot (d_s/d_{50})^{0.028} \cdot K_0^{-0.218} \,. \tag{C.3}$$

The linearised model fit, visualised in Fig. C.19, was statistically significant overall ($p < 0.01$) with an adjusted $R^2 \approx 0.738$. Note that this equation is valid only for the specific range of parameters and soil types simulated in this study and should be applied with caution outside these bounds. Therefore, this equation should be viewed as a qualitative trend analysis rather than a predictive design tool. However, the statistical analysis successfully highlights the dominant influence of the interface roughness κ as a highly significant predictor of Π_P. The statistical insignificance of I_D, d_s/d_{50}, and K_0 suggests that their primary physical influence is effectively captured by the normalisation used in Eq. (C.1).

C.3. Simplified dimensional equation

To avoid overfitting and create a more robust, simple model, the terms with low impact (I_D and d_s/d_{50}) were removed. By substituting the definition of Π_P from Eq. (C.1) into the simplified model and rearranging the terms, a final dimensional equation for pull-out capacity is obtained. The exponents for the earth pressure coefficient are combined ($K_0^{-0.218} \cdot K_0^{1.0} = K_0^{0.782}$), yielding:

$$P_{ult} \approx 0.42 \cdot \kappa^{0.39} \cdot K_0^{0.782} \cdot \gamma'_{sands,avg} \cdot \left(\frac{L^2}{2}\right) \cdot U_{profile} \,. \tag{C.4}$$

C.4. Discussion and limitations

The dimensionless constant $C \approx 0.42$ can be interpreted as a mobilised friction coefficient. This value is slightly higher than the simple $\tan(\delta_{mob}) \approx 0.38$ calculated for the baseline case, which may reflect complex mechanisms for H-piles not captured by simple friction, such as soil interlock between flanges. This formulation provides a more fundamentally grounded relationship than a simple empirical fit. However, its derivation relies on an OFAT methodology using synthetic FEM data, which precludes assessing parameter interactions. While the dimensionless constant C is expected to be more robust than a purely dimensional coefficient, its universal applicability requires further comparison against a broader range of conditions. Verification of the proposed relationship is recommended for new sites.

Data availability

Data will be made available on request.

References

Al-Kafaji, I.K.J., 2013. Formulation of a Dynamic Material Point Method (MPM) for Geomechanical Problems (Ph.D. thesis). University of Stuttgart. Ridderprint BV, URL: https://elib.uni-stuttgart.de/handle/11682/513.

Alkateeb, D., Grabe, J., 2022. On the application of analytical methods and empirical values for the determination of the pull-out resistance of driven steel piles. In: Proceedings of 10th International Conference on Physical Modelling in Geotechnics (ICPMG) 2022 in Daejeon/Korea. Korea Geotechnical Society, pp. 844–848.

Alkateeb, D., Grabe, J., 2026. Bearing capacity of tension steel piles in thinly interlayered soils: Numerical Class-A Prediction vs. Field measurements. Int. J. Numer. Anal. Methods Geomech. 50 (3), 1430–1450. http://dx.doi.org/10.1002/nag.70132, URL: https://onlinelibrary.wiley.com/doi/abs/10.1002/nag.70132.

Ampera, B., Aydogmus, T., 2005. Skin friction between peat and silt soils with construction materials. Electron. J. Geotech. Eng. 10.

Arnold, M., 2008. Application of the intergranular strain concept to the hypoplastic modelling of non-adhesive interfaces. In: Singh, D.N. (Ed.), Proceedings of the 12th International Association for Computer Methods and Advances in Geomechanics (IACMAG) Conference. Goa, India, pp. 747–754.

Arnold, M., Herle, I., 2006. Hypoplastic description of the frictional behaviour of contacts. In: Schweiger, H. (Ed.), Proceedings of the 6th European Conference on Numerical Methods in Geotechnical Engineering. pp. 101–106. http://dx.doi.org/10.1201/9781439833766.ch14.

Axelsson, G., 2000. Long-Term Set-Up of Driven Piles in Non-Cohesive Soils (Ph.D. thesis). Royal Institute of Technology, Division of Soil and Rock Mechanics, Department of Civil and Environmental Engineering, Stockholm.

Bathe, K.-J., 2006. Finite Element Procedures. Massachusetts Institute of Technology, Cambridge, Massachusetts.

Benson, D.J., 1992. Computational methods in Lagrangian and Eulerian hydrocodes. Comput. Methods Appl. Mech. Engrg. 99, 235–394. http://dx.doi.org/10.1016/0045-7825(92)90042-I.

Bienen, B., Fan, S., Schröder, M., Randolph, M.F., 2021. Effect of the installation process on monopile lateral response. Proc. Inst. Civ. Eng. - Geotech. Eng. 174, 530–548. http://dx.doi.org/10.1680/jgeen.20.00219.

Boulbes, R.J., 2020. Troubleshooting Finite-Element Modeling with Abaqus: With Application in Structural Engineering Analysis. Springer Nature Switzerland AG, ISBN: 978-3-030-26740-7, http://dx.doi.org/10.1007/978-3-030-26740-7.

Brumund, W., Leonards, G., 1973. Experimental study of static and dynamic friction between sand and typical construction materials. J. Test. Eval. 1, 162–165.

Canakci, H., Hamed, M., Celik, F., Sidik, W., Eviz, F., 2016. Friction characteristics of organic soil with construction materials. Soils Found. 56, 965–972. http://dx.doi.org/10.1016/j.sandf.2016.11.002.

Chow, F.C., Jardine, R.J., Nauroy, J.F., Brucy, F., 1997. Time-related increase in shaft capacities of driven piles in sand. Géotechnique 47, 353–361.

Clough, G., Duncan, J., 1971. Finite element analyses of retaining wall behaviour. J. Soil Mech. Found. Div. 1657–1673. http://dx.doi.org/10.1061/JSFEAQ.0001713.

Cola, S., Cortellazzo, G., 2005. The shear strength behavior of two peaty soils. Geotech. Geol. Eng. 23, 679–695. http://dx.doi.org/10.1007/s10706-004-9223-9.

Costa D Aguiar, S., Modaressi-Farahmand-Razavi, A., dos Santos, J., Lopez-Caballero, F., 2011. Elastoplastic constitutive modelling of soil-structure interfaces under monotonic and cyclic loading. Comput. Geotech. 38, 430–447. http://dx.doi.org/10.1016/j.compgeo.2011.02.006.

Dao, D.A., Alkateeb, D., Schröder, M., 2023. Discrepancies between element tests and large-scale LDFE simulations: A case study on anchor kinematics during installation in clay. Comput. Geotech. 163, 105698. http://dx.doi.org/10.1016/j.compgeo.2023.105698.

Dao, D.A., Grabe, J., 2024. Numerical assessment of ship anchor penetration depth in Baltic Sea Sand: Implications for subsea cable burial. Ocean Eng. 314, 119674. http://dx.doi.org/10.1016/j.oceaneng.2024.119674.

Dassault Systèmes, 2022. Abaqus analysis user's manual.

DeJong, J.T., Westgate, Z.J., 2009. Role of initial state, material properties, and confinement condition on local and global soil-structure interface behavior. J. Geotech. Geoenvironmental Eng. 135, 1646–1660. http://dx.doi.org/10.1061/(ASCE)1090-0241(2009)135:11(1646).

DeJong, J.T., White, D.J., Randolph, M.F., 2006. Microscale observation and modeling of soil-structure interface behavior using particle image velocimetry. Soils Found. 46, 15–28. http://dx.doi.org/10.3208/sandf.46.15.

DIN 4085:2017-08, 2017. Baugrund - Berechnung Des Erddrucks. Standard, Beuth Verlag GmbH, Germany.

Duriez, J., Vincens, É., 2015. Constitutive modelling of cohesionless soils and interfaces with various internal states: An elasto-plastic approach. Comput. Geotech. 63, 33–45. http://dx.doi.org/10.1016/j.compgeo.2014.08.001.

EA-Pfähle, 2013. Recommendations on Piling (EA-Pfähle), first ed. Wiley, http://dx.doi.org/10.1002/9783433604113.

EAU 2020, 2023. Recommendations of the Committee for Waterfront Structures Harbours and Waterways: EAU 2020, tenth ed. Wilhelm Ernst & Sohn, Berlin, Germany, Published by Wilhelm Ernst & Sohn on behalf of the HTG (Hafentechnische Gesellschaft e.V.) and DGGT (Deutsche Gesellschaft für Geotechnik e.V.).

Edil, T.B., Dhowian, A.W., 1981. At-rest lateral pressure of peat soils. J. Geotech. Eng. Div. ASCE 107, 201–217. http://dx.doi.org/10.1061/AJGEB6.0001097.

Fakharian, K., Evgin, E., 2000. Elasto-plastic modelling of stress-path dependent behaviour of interfaces. Int. J. Numer. Anal. Methods Geomech. 24, 183–199. http://dx.doi.org/10.1002/(SICI)1096-9853(200002)24:2<183::AID-NAG63>3.0.CO;2-3.

Gennaro, V., Frank, R., 2002. Elasto-plastic analysis of the interface behaviour between granular media and structure. Comput. Geotech. 29, 547–572. http://dx.doi.org/10.1016/S0266-352X(02)00010-1.

Gens, A., Carol, I., Alonso, E.E., 1989. An interface element formulation for the analysis of soil-reinforcement interaction. Comput. Geotech. 7, 133–151. http://dx.doi.org/10.1016/0266-352X(89)90011-6.

Ghionna, V., Mortara, G., 2002. An elastoplastic model for sand–structure interface behaviour. Géotechnique 52, 41–50. http://dx.doi.org/10.1680/geot.2002.52.1.41.

Gómez, J., Filz, G., Ebeling, R., 2003. Extended hyperbolic model for sand-to-concrete interfaces. J. Geotech. Geoenvironmental Eng. 129, 993–1000. http://dx.doi.org/10.1061/(ASCE)1090-0241(2003)129:11(993).

Grabe, J., Busch, P., Hamann, T., 2014. On the set-up of piles. In: International Conference on Offshore Mechanics and Arctic Engineering. http://dx.doi.org/10.1115/OMAE2014-24433.

Gutjahr, S., 2003. Optimierte Berechnung von Nicht Gestützten Baugrubenwänden in Sand (Ph.D. thesis). Lehrstuhl Baugrund-Grundbau, TU Dortmund / Technische Universität Dortmund, Dortmund.

Hamid, T., Miller, G., 2008. A constitutive model for unsaturated soil interfaces. Int. J. Numer. Anal. Methods Geomech. 32, 1693–1714. http://dx.doi.org/10.1002/nag.692.

Herle, I., Nübel, K., 1999. Hypoplastic description of the interface behaviour. In: Pande, G.N., Pietruszczak, S., Schweiger, H.F. (Eds.), Numerical Models in Geomechanics. Proceedings of the 7th International Symposium, Graz, September 1999. pp. 53–58.

Hu, L., Pu, J., 2003. Application of damage model for soil-structure interface. Comput. Geotech. 30, 165–183. http://dx.doi.org/10.1016/S0266-352X(02)00059-9.

Hu, L., Pu, J., 2004. Testing and Modeling of soil-structure interface. J. Geotech. Geoenvironmental Eng. 130, 851–860. http://dx.doi.org/10.1061/(ASCE)1090-0241(2004)130:8(851).

Jaky, J., 1948. Pressure in silos. In: Proc. 2nd International Conference on Soil Mechanics and Foundation Engineering. pp. 103–107.

Kencana, E., Haryono, I., Leung, C., Chow, Y., 2021. Mass-gravity-scaling technique to enhance computational efficiency of explicit numerical methods for quasi-static problems. Comput. Geotech. 133, 103999. http://dx.doi.org/10.1016/j.compgeo.2021.103999.

Kulhawy, F.H., Mayne, P.H., 1990. Manual on Estimating Soil Properties for Foundation Design. Electric Power Research Institute.

Lashkari, A., 2013. Prediction of the shaft resistance of nondisplacement piles in sand. Int. J. Numer. Anal. Methods Geomech. 37, 904–931. http://dx.doi.org/10.1002/nag.1129.

Lings, M., Dietz, M., 2005. The peak strength of sand-steel interfaces and the role of dilation. Soils Found. 45, 1–14. http://dx.doi.org/10.3208/sandf.45.1, URL: https://www.sciencedirect.com/science/article/pii/S0038080620309069.

Liu, H., Ling, H., 2008. Constitutive description of interface behavior including cyclic loading and particle breakage within the framework of critical state soil mechanics. Int. J. Numer. Anal. Methods Geomech. 32, 1495–1514. http://dx.doi.org/10.1002/nag.682.

Liu, H., Song, E., Ling, H., 2006. Constitutive modeling of soil-structure interface through the concept of critical state soil mechanics. Mech. Res. Commun. 33, 515–531. http://dx.doi.org/10.1016/j.mechrescom.2006.01.002.

Liu, J., Zou, D., Kong, X., 2014. A three-dimensional state-dependent model of soil-structure interface for monotonic and cyclic loadings. Comput. Geotech. 61, 166–177. http://dx.doi.org/10.1016/j.compgeo.2014.05.012.

Maier, T., 2002. Numerische Modellierung Der Entfestigung Im Rahmen Der Hypoplastizität (Ph.D. thesis). Lehrstuhl Baugrund-Grundbau, Universität Dortmund / Universität Dortmund, Dortmund.

Martinez, A., Frost, J.D., Hebeler, G.L., 2015. Experimental Study of Shear Zones Formed at Sand/Steel Interfaces in Axial and torsional axisymmetric tests. Geotech. Test. J. 38, 409–426. http://dx.doi.org/10.1520/GTJ20140266.

Mesri, G., Ajlouni, M., 2007. Engineering properties of fibrous peats. J. Geotech. Geoenvironmental Eng. 133, 850–866. http://dx.doi.org/10.1061/(ASCE)1090-0241(2007)133:7(850).

Nakayama, H., 2006. Modelling Interfaces Between Sand and Structural Elements (Ph.D. thesis). University of Bristol.

Navayogarajah, N., Desai, C., Kiousis, P., 1992. Hierarchical single surface model for static and cyclic behavior of interfaces. J. Eng. Mech. 118, 990–1011. http://dx.doi.org/10.1061/(ASCE)0733-9399(1992)118:5(990).

Niebler, M., Chrisopoulos, S., Cudmani, R., Rebstock, D., 2025. A general framework to simulate soil–structure interface behaviour using advanced constitutive models. Modelling 6, http://dx.doi.org/10.3390/modelling6010011.

Niemunis, A., Herle, I., 1997. Hypoplastic model for cohesionless soils with elastic strain range. Mech. Cohesive-Frictional Mater. 2, 279–299. http://dx.doi.org/10.1002/(SICI)1099-1484(199710)2:4<279::AID-CFM29>3.0.CO;2-8.

Osthoff, D., Grabe, J., 2018. Deformational behaviour of steel sheet piles during jacking. Comput. Geotech. 101, 1–10. http://dx.doi.org/10.1016/j.compgeo.2018.04.014.

Randolph, M.F., 2003. Science and empiricism in pile foundation design. Géotechnique 53, 847–875.

Samtani, N., Desai, C., Vulliet, L., 1996. An interface model to describe viscoplastic behavior. Int. J. Numer. Anal. Methods Geomech. 20, 231–252. http://dx.doi.org/10.1002/(SICI)1096-9853(199604)20:4<231::AID-NAG816>3.0.CO;2-E.

Shahrour, I., Rezaie, F., 1997. An elastoplastic constitutive relation for the soil-structure interface under cyclic loading. Comput. Geotech. 21, 21–39. http://dx.doi.org/10.1016/S0266-352X(97)00001-3.

Shao, R., Desai, C., 2000. Implementation of DSC model and application for analysis of field pile tests under cyclic loading. Int. J. Numer. Anal. Methods Geomech. 24, 601–624. http://dx.doi.org/10.1002/(SICI)1096-9853(200005)24:6<601::AID-NAG85>3.0.CO;2-3.

Skov, R., 1997. Pile foundation — Danish design methods and piling practice. In: Design of Axially Loaded Piles - European Practice. CRC Press.

Stapelfeldt, M., Alkateeb, D., Grabe, J., Bienen, B., 2020. Numerical simulation of cone penetration tests inside suction caisson foundations in sand. In: Proceedings of the ASME 2020 39th International Conference on Ocean, Offshore and Arctic Engineering. OMAE2020, American Society of Mechanical Engineers (ASME), V010T10A007. http://dx.doi.org/10.1115/OMAE2020-18721.

Staubach, P., Machaček, J., Wichtmann, T., 2022a. Impact of the constitutive contact model on the simulation of model tests on monopiles with high-cyclic loading. In: Proceedings of the 20th International Conference on Soil Mechanics and Geotechnical Engineering. Sydney, pp. 2685–2690.

Staubach, P., Machaček, J., Wichtmann, T., 2022b. Mortar contact discretisation methods incorporating interface models based on Hypoplasticity and Sanisand: Application to vibratory pile driving. Comput. Geotech. 146, 104677. http://dx.doi.org/10.1016/j.compgeo.2022.104677.

Staubach, P., Machaček, J., Wichtmann, T., 2022c. Novel approach to apply existing constitutive soil models to the modelling of interfaces. Int. J. Numer. Anal. Methods Geomech. 46, 1241–1271. http://dx.doi.org/10.1002/nag.3344.

Stutz, H., 2016. Hypoplastic Models for Soil-Structure Interfaces: Modelling and Implementation (Ph.D. thesis). Faculty of Mathematics and Natural Sciences at Kiel University.

Stutz, H., Mašín, D., Sattari, A., Wuttke, F., 2017. A general approach to model interfaces using existing soil constitutive models application to hypoplasticity. Comput. Geotech. 87, 115–127. http://dx.doi.org/10.1016/j.compgeo.2017.02.010.

Stutz, H., Mašín, D., Wuttke, F., 2016. Enhancement of a hypoplastic model for granular soil–structure interface behaviour. Acta Geotech. 11, 1249–1261. http://dx.doi.org/10.1007/s11440-016-0440-1.

Stutz, H.H., Wuttke, F., 2018. Hypoplastic modeling of soil-structure interfaces in offshore applications. J. Zhejiang Univ. - Sci. A 19, 624–637. http://dx.doi.org/10.1631/jzus.A1700469.

Subba Rao, K.S., Allam, M.M., Robinson, R.G., 1998. Interfacial friction between sands and solid surfaces. Proc. Inst. Civ. Eng. - Geotech. Eng. 131, 75–82. http://dx.doi.org/10.1680/igeng.1998.30112.

Teichmann, J., 1989. Scherzonenbildung Und Verspannungseffekte in Granulaten Unter Berücksichtigung Von Korndrehungen (Ph.D. thesis). Institut für Bodenmechanik und Felsmechanik, Universität Karlsruhe / Universität Fridericiana Karlsruhe, Karlsruhe.

Tejchman, J., Wu, W., 1995. Experimental and numerical study of sand–steel interfaces. Int. J. Numer. Anal. Methods Geomech. 19, 513–536. http://dx.doi.org/10.1002/nag.1610190803.

U.S. Army Corps of Engineers, 1991. Design of Pile Foundations. Department of the Army, Washington, DC.

von Wolffersdorff, P.A., 1996. A hypoplastic relation for granular materials with a predefined limit state surface. Mech. Cohesive-Frict. Mater. 1, 251–271. http://dx.doi.org/10.1002/(SICI)1099-1484(199607)1:3<251::AID-CFM13>3.0.CO;2-3.

Weißenfels, C., Harish, A.B., Wriggers, P., 2017. Strategies to apply soil models directly as friction laws in soil structure interactions. In: Holistic Simulation of Geotechnical Installation Processes: Theoretical Results and Applications. Springer International Publishing, Cham, pp. 216–236. http://dx.doi.org/10.1007/978-3-319-52590-7_9.

Weißenfels, C., Wriggers, P., 2015. Methods to project plasticity models onto the contact surface applied to soil structure interactions. Comput. Geotech. 65, 187–198. http://dx.doi.org/10.1016/j.compgeo.2014.11.015.

Yamaguchi, Y., Ohira, Y., Kogure, K., Mori, S., 1985. Undrained shear characteristics of normally consolidated peat under triaxial compression and extension conditions. Soils Found. 25, 1–18. http://dx.doi.org/10.3208/sandf1972.25.3_1.

Yang, Z., Li, X., Yang, J., 2008. Interpretation of torsional shear results for nonlinear stress–strain relationship. Int. J. Numer. Anal. Methods Geomech. 32, 1247–1266. http://dx.doi.org/10.1002/nag.669.

Ziccarelli, M., 2024. The coefficient of earth pressure at rest k0 of sands up to very high stresses. Geosciences 14, http://dx.doi.org/10.3390/geosciences14100264, URL: https://www.mdpi.com/2076-3263/14/10/264.